NASA/CR–2013-218003

A Comprehensive Structural Dynamic Analysis Approach for Multi Mission Earth Entry Vehicle (MMEEV) Development

Scott Perino, Javid Bayandor, and Aaron Siddens
Crashworthiness for Aerospace Structures and Hybrids (CRASH) Laboratory
Department of Mechanical Engineering
Blacksburg, Virginia

June 2012

NASA STI Program . . . in Profile

Since its founding, NASA has been dedicated to the advancement of aeronautics and space science. The NASA scientific and technical information (STI) program plays a key part in helping NASA maintain this important role.

The NASA STI program operates under the auspices of the Agency Chief Information Officer. It collects, organizes, provides for archiving, and disseminates NASA's STI. The NASA STI program provides access to the NASA Aeronautics and Space Database and its public interface, the NASA Technical Report Server, thus providing one of the largest collections of aeronautical and space science STI in the world. Results are published in both non-NASA channels and by NASA in the NASA STI Report Series, which includes the following report types:

- TECHNICAL PUBLICATION. Reports of completed research or a major significant phase of research that present the results of NASA Programs and include extensive data or theoretical analysis. Includes compilations of significant scientific and technical data and information deemed to be of continuing reference value. NASA counterpart of peer-reviewed formal professional papers, but having less stringent limitations on manuscript length and extent of graphic presentations.

- TECHNICAL MEMORANDUM. Scientific and technical findings that are preliminary or of specialized interest, e.g., quick release reports, working papers, and bibliographies that contain minimal annotation. Does not contain extensive analysis.

- CONTRACTOR REPORT. Scientific and technical findings by NASA-sponsored contractors and grantees.

- CONFERENCE PUBLICATION. Collected papers from scientific and technical conferences, symposia, seminars, or other meetings sponsored or co-sponsored by NASA.

- SPECIAL PUBLICATION. Scientific, technical, or historical information from NASA programs, projects, and missions, often concerned with subjects having substantial public interest.

- TECHNICAL TRANSLATION. English-language translations of foreign scientific and technical material pertinent to NASA's mission.

Specialized services also include organizing and publishing research results, distributing specialized research announcements and feeds, providing information desk and personal search support, and enabling data exchange services.

For more information about the NASA STI program, see the following:

- Access the NASA STI program home page at *http://www.sti.nasa.gov*

- E-mail your question to help@sti.nasa.gov

- Fax your question to the NASA STI Information Desk at 443-757-5803

- Phone the NASA STI Information Desk at 443-757-5802

- Write to:
  STI Information Desk
  NASA Center for AeroSpace Information
  7115 Standard Drive
  Hanover, MD 21076-1320

NASA/CR–2013-218003

A Comprehensive Structural Dynamic Analysis Approach for Multi Mission Earth Entry Vehicle (MMEEV) Development

Scott Perino, Javid Bayandor, and Aaron Siddens
Crashworthiness for Aerospace Structures and Hybrids (CRASH) Laboratory
Department of Mechanical Engineering
Blacksburg, Virginia

National Aeronautics and
Space Administration

Langley Research Center
Hampton, Virginia 23681-2199

Prepared for Langley Research Center
under Contract NNL09AA00Z

June 2012

Available from:

NASA Center for AeroSpace Information
7115 Standard Drive
Hanover, MD 21076-1320
443-757-5802

Abstract

The anticipated NASA Mars Sample Return Mission (MSR) requires a simple and reliable method in which to return collected Martian samples back to earth for scientific analysis. The Multi-Mission Earth Entry Vehicle (MMEEV) is NASA's proposed solution to this MSR requirement. Key aspects of the MMEEV are its reliable and passive operation, energy absorbing foam-composite structure, and modular impact sphere (IS) design. To aid in the development of an EEV design that can be modified for various missions requirements, two fully parametric finite element models were developed. The first model was developed in an explicit finite element code and was designed to evaluate the impact response of the vehicle and payload during the final stage of the vehicle's return to earth. The second model was developed in an explicit code and was designed to evaluate the static and dynamic structural response of the vehicle during launch and reentry. In contrast to most other FE models, built through a Graphical User Interface (GUI) pre-processor, the current model was developed using a coding technique that allows the analyst to quickly change nearly all aspects of the model including: geometric dimensions, material properties, load and boundary conditions, mesh properties, and analysis controls. Using the developed design tool, a full range of proposed designs can quickly be analyzed numerically and thus the design trade space for the EEV can be fully understood. An engineer can then quickly reach the best design for a specific mission and also adapt and optimize the general design for different missions.

Table of Contents

List of Figures

List of Tables

Introduction

Throughout space exploration history much effort has been spent on collecting and testing extraterrestrial materials. Numerous lunar samples have been collected since the Apollo missions and there is currently a desire to learn more about our universe by collecting samples from other planets. To date, the information obtained on Mars and other planets has been through the use of rovers, sattelites and orbital space modules with in-situ testing devices. However, some information about materials and gases can be obtained exclusively through the use of advanced equipment only available on earth. A new reliable way to return samples is therefore needed. Due to the overall complexity of the Mars Sample Return Mission (MSR), a very simple and reliable earth entry vehicle (EEV) with passive reentry design is desired and has been devised[1]. The proposed design shown in Fig. 1 has no complicated parachute system and relies entirely on atmospheric aerodynamic drag during reentry and an impact absorbing sphere designd to reduce impact velocities and accelerations down to levels where containment and survival of the enclosed material samples can be nearly guaranteed.

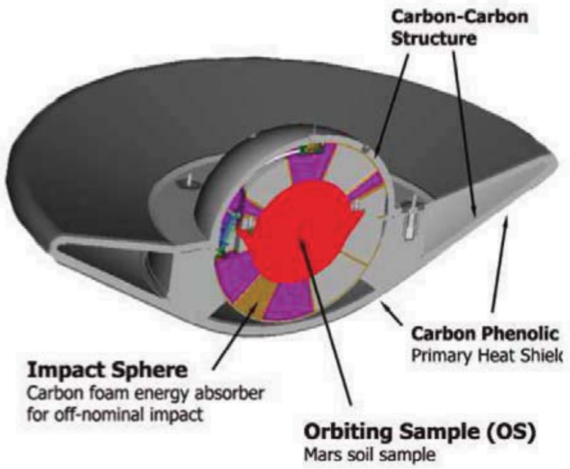

Figure 1: MSR Earth Entry Vehicle [2]

The parametric design tool developed is a key part of the "Integrated Tool for System Analysis of Sample Return Vehicles" in Ref. 3. The methodology for developing such as tool has been discussed by Bayandor et al. in Ref. 15. With respect to being considered design tools, most finite element (FE) models are severely limited in that they are often hard to modify, particularly geometrically. Since graphical user interface (GUI) based FE codes have become popular, FE models are mostly built by clicking the menu options within the FE program in the correct sequential manner. Quite often when using this method of model development, it is hard to back tract once two or more design decision have been made. In contrast to such limitations, the system dynamics model described in this report was developed using a coding technique that allows the analyst to quickly change nearly all aspects of the model including geometric dimensions, material properties, load and boundary conditions, mesh definitions, and analysis controls. Furthermore, once the analyst has defined the model parameters, the submission of all required analyses is automated and thus can be conducted with a single command. Given the proper computational resources, the developed model can be used to rapidly generate data for thousands of potential EEV design variations.

Multi-Mission Earth Entry Vehicle

The multi-mission earth entry vehicle MMEEV is designed to be a stand-alone, modifiable earth entry platform that can be tailored for different missions with different payload requirements. One key design feature is its simple and reliable passive reentry design, where no complicated and potentially unreliable velocity reducing subsystems such as parachutes or boosters are used.

A typical EEV mission scenario is depicted in Fig. 2 from Ref. 16. First a preliminary misssion sends a rover and other equipement to Mars in order to collect Martian samples. The samples are then collected and sealed in an Orbiting Sphere (OS). The OS is then launched from Mars back towards Earth aboard a Mars Ascent Vehicle (MAV). Separetely an empty EEV, attached to an orbiter, is launched into orbit via a launch vehicle such as a Delta VI or Atlas V rocket. Once in orbit, the orbiter (shown in Fig. 26) and EEV wait to rendevous with the rocket from Mars carrying the OS. Once the OS arrives at the orbiter, the OS is loaded and sealed inside the EEV. After sample containment is assured, the the EEV is released into the earth's atmosphere for return to earth. During reentry, the vehicle's speed is reduced to the vehicle's terminal velocity of approximately 40m/s before impacting on the soft soil in approved fields such as the Utah Training and Testing Range[5]. For the mission to be successful, the EEV must be able to land without the samples being destroyed or contaminated[4]. Although thermal issues due to atmospheric heating may be an issue, they are not currently addressed by the developed model. This is because the focus of the current model is capturing the structural response of the EEV.

As shown in Fig. 1, the vehicle is comprised of four basic components. At the center of the vehicle is the orbiting sample/sphere (OS) which is a metallic sphere that holds the extraterrestrial soil samples. Next, encapsulating the OS, is the impact sphere (IS), which is used to protect the orbiting sphere and soil samples when the vehicle hits the earth. Holding the IS and OS is the primary structure which is designed to withstand structural and thermal loads on the vehicle during launch and reentry. Finally, surrounding the exterior of the vehicle is a thermal protection shield (TPS), which resists the high heat generated during reentry into the earth's atmosphere and thermally protects all the interior components.

The OS is composed of two sections, an upper and lower part that seal against each other and allow the sphere to be opened and samples to be inserted within the sphere while in orbit around the earth. The OS is built of a metallic and relatively rigid material. The impact sphere is a spherically shaped, passive impact energy absorber designed to crush on impact and resist penetration. The design of the IS was provided by Kellas in a previous NASA report[4]. The IS is constructed of hybrid composite (carbon and Kevlar) materia

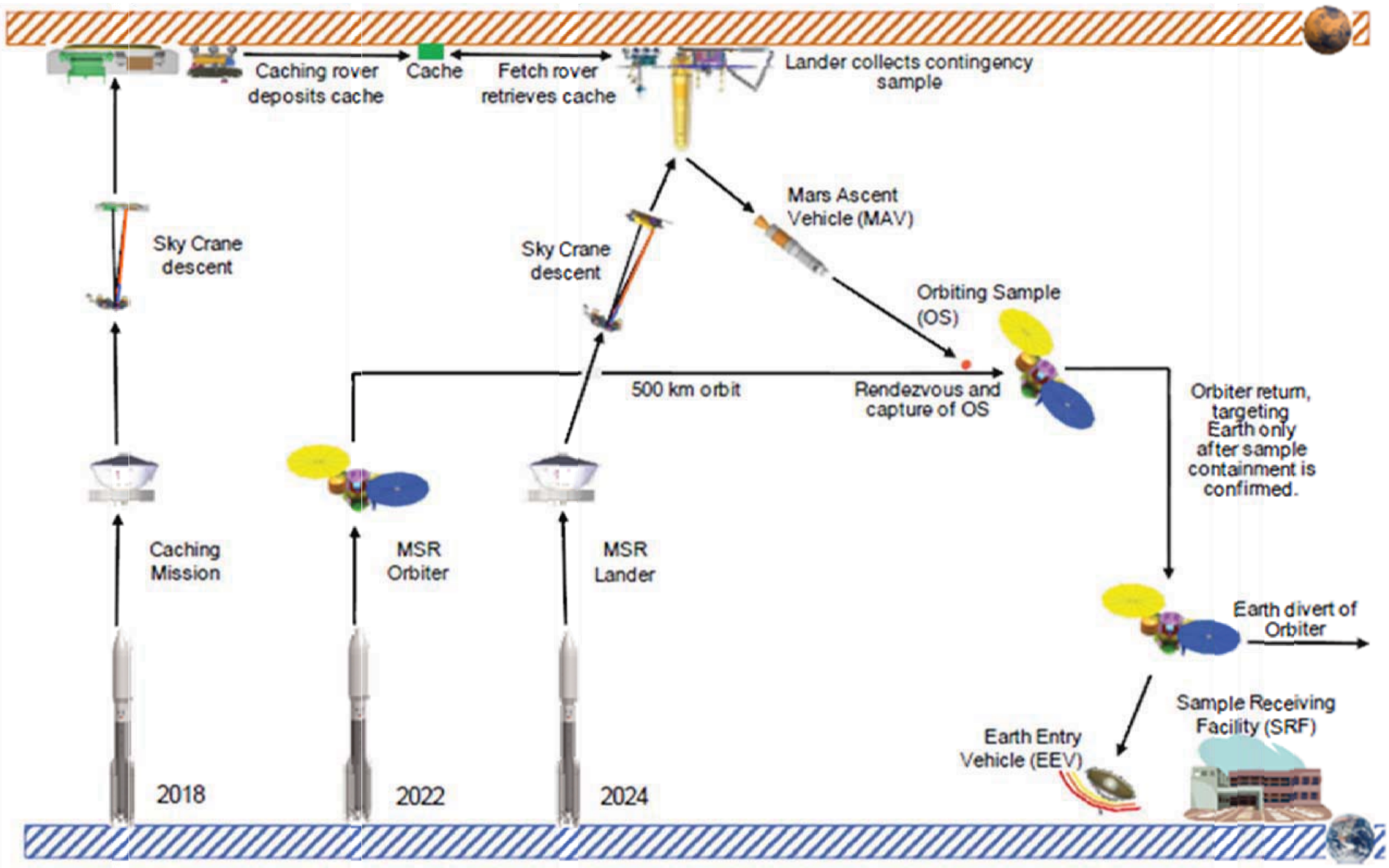

Figure 2: Mars Sample Return mission schematic[16]

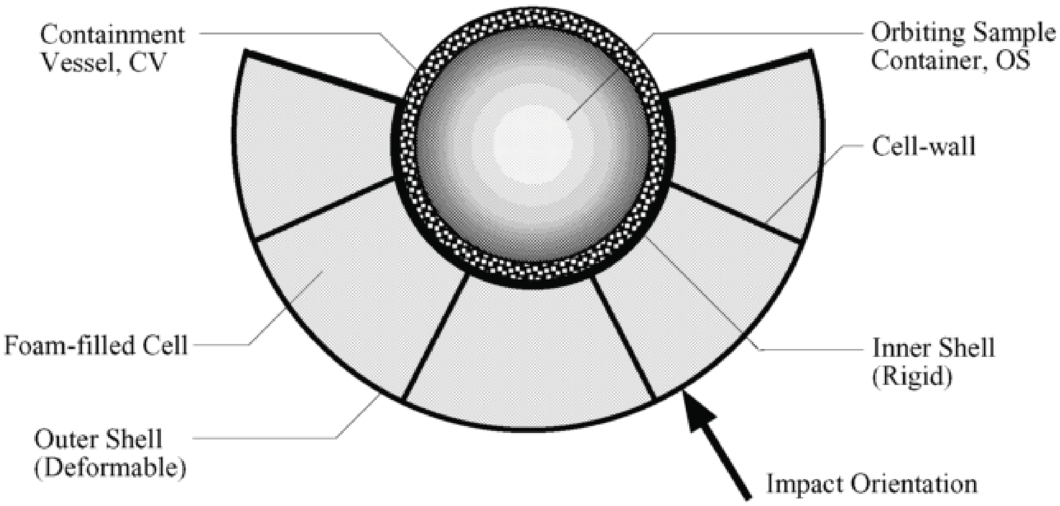

Figure 2: Schematic of Impact Sphere sub-components[4]

and crushable foam. The IS schematic, shown in Fig. 3, encapsulates the OS and is composed of five sub components each with a primary purpose. An inner shell made of carbon fiber composite is designed to distribute impact forces evenly on the OS. Crushable foam cells in both hexagonal and pentagonal shape are designed to crush as well as brace the composite cell walls that wrap each foam cell during impact. The carbon-Kevlar composite cell walls that surround each foam cell are designed to crimple (locally buckle) in order to absorb the most amount of energy during impact. A carbon-Kevlar composite outer shell is designed to spread out the impact load internally and resist foreign object penetration during impact. Lastly a containment vessel is made of loose plies for Kevlar and is intended as a buffer between the IS and OS as well as a last line of defense against penetration. The four components are assembled into what looks from the outside like a soccer ball with a smoothened surface and then co-cured in a technique described in Ref. 4. It can be seen that once assembled and cured, each foam cell is enclosed on all sides by composite material. All components are designed to work together to maximize impact energy absorption and to minimize peak accelerations at the OS.

Impact Model Design

Experimental tests on several different IS configurations have been conducted at the NASA Langley Research Center (LaRC)[4]. During the tests, IS prototypes were impacted without any primary structure or TPS components. When developing the impact model, it was expected that the TPS and primary structure components of the EEV would have a small influence on the overall impact response of the vehicle. Thus, to accurately match and validate the model against test data as well as to reduce simulation computation time, the primary structure and TPS components were not modeled in the simulations.

The impact model is composed of a rigid plate that has been fixed in all three translational degrees of freedom and an IS that has been placed approximately 1mm from the surface of the plate. The entire IS has been assigned an initial velocity vector perpendicular to the face of the rigid plate. Once the simulation begins, the IS moves toward the plate almost immediately making contact with the plate. After initial contact, the IS deforms, causing large deformations and failure of both foam and composite shell elements. At 2-3ms, the IS rebounds off the rigid surface. The simulation runs for a total of 4ms and then terminates. A gravitational force is the only external forces applied to the model during the simulation. The output data principally of interest is the displacement, velocity and acceleration information found at the OS.

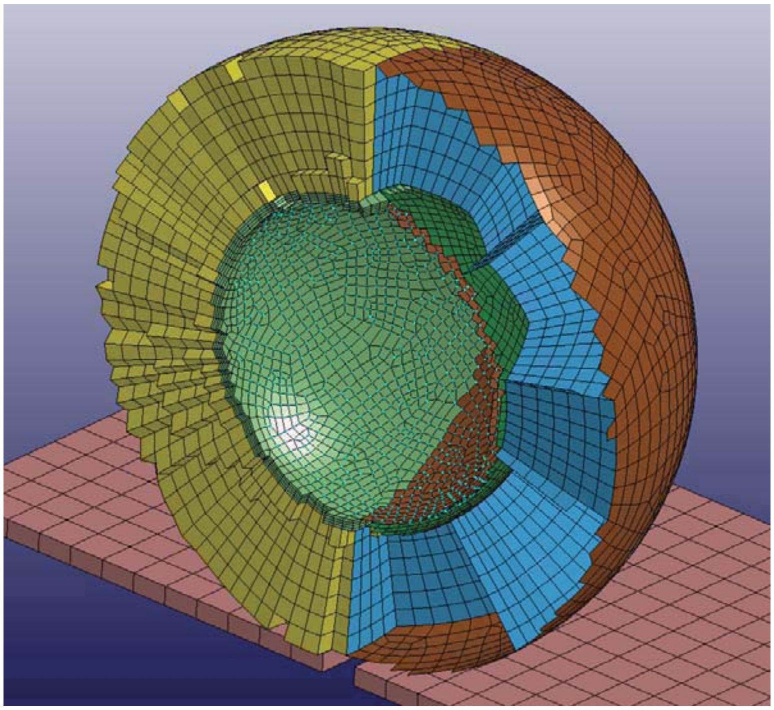

Figure 3: Biplane cross section view of the impact model showing each subcomponent

In previous EEV simulation work by Bauer et al., the impact surface was modeled to be the Utah desert sand[5]. However, for this work, it was decided through collaboration with NASA engineers to focus on the most severe flat surface impact scenario, which is represented by a hard rigid surface such as a cemented road section. For qualification purposes 3500g's was determined to be the peak allowable acceleration inside of the OS on impact onto a hard surface[4].

The model shown in figure three is a double cross sectional view with elements hidden so that all components can be clearly visible in a single image. The model has eight element sets, three of the element sets are solid element sets, four are shell element sets, and one is a mass element set. The three solid element sets are the rigid impact surface shown in pink, the crushable foam element set shown in yellow, and the Control Volume (CV) element set shown in pale green. The shell element sets are the outer shell set shown in brown, the cell wall set shown in blue, the inner shell set shown in dark green, and the OS set shown at the very inside of the sphere also in brown. The mass element set is hard to see in the image but one mass element is attached to each node on the OS shell surface at the very interior of the IS. The mass elements render as pale blue dots on the OS shell element surface.

The model consists of a total of 59,731 elements. Of this total 40,005 are solid elements, primarily found in the crushable foam and CV components, 15150 elements are shell elements mostly placed in the outer shell, inner shell, and cell wall components, and 3576 are mass elements attached to the OS nodes. The mass elements are present so that the model mass can be set equal to the mass of specimens used in experimental tests.

Table 1. Composite Material Properties

	Cell Walls		Outer Sphere		Inner Sphere	
Material Model	055-ENHANCED_COMPOSITE_DAMAGE					
E11	1.38E+10	Pa	6.90E+09	Pa	4.55E+10	Pa
E22	1.38E+10	Pa	6.90E+09	Pa	4.55E+10	Pa
G12	5.30E+09	Pa	2.65E+09	Pa	1.75E+10	Pa
G23	5.30E+09	Pa	2.65E+09	Pa	1.75E+10	Pa
G13	5.30E+09	Pa	2.65E+09	Pa	1.75E+10	Pa
S11t,S22t	3.65E+08	Pa	1.03E+08	Pa	5.59E+08	Pa
S11c,S22c	7.60E+07	Pa	1.03E+08	Pa	1.10E+08	Pa
Density	1.25E+03	kg/m^2	1.38E+03	kg/m^2	1.55E+03	kg/m^2
Poison's Ratio	0.3		0.3		0.3	

Table 2. Composite Shell Element Thicknesses and Layups used for Simulation

	Cell Walls Ply Seq.	Cell Wall Thickness (mm)	Inner Sphere Ply Seq.	Inner Sphere Thickness (mm)	Outer Sphere Ply Seq.	Outer Sphere Thickness (mm)
Test 2	$(Gp_5/Kp)_S$	2.080	Gp_3	0.780	Kp_2	0.520
Test 4b	$(Gp_7/Kp_2)_S$	4.750	Gp_2	2.300	$Gp/Kp_2/Gs_2$	1.750

The model was formulated to be consistent in some ways with a previous simulation work by Billings[6] and experimental test data conducted at NASA[4]. As with previous models, the developed model assumes perfect union between all subcomponents that are in direct contact with each other, thus all coincident nodes from different subcomponents have been merged. Of all the components that have merged nodes, the most significant connection is the union between the OS and the CV. Test data from the Kellas report suggests that a small gap may have been present in many of the specimens. This small gap is very difficult to remove, particularly in space, and has shown to lead to spikes in the acceleration time response curves. Fortunately, the 3500g maximum peak acceleration criterion mentioned previously is conservative and is intended to take this issue into consideration.

The impact model was designed to allow for the maximum level of parametric customization and ease of change by engineers in the future. The impact response of the EEV depends strongly on the composite laminate properties and element formulation. Therefore, extra features have been added that allow full parameterization of the composite layup and material properties. The model at this point uses a single ply quasi-isotropic laminate since the directionality of each bi-axial braided layer of fabric is not well characterized by the manufacturing process[4]. Laminate level material properties

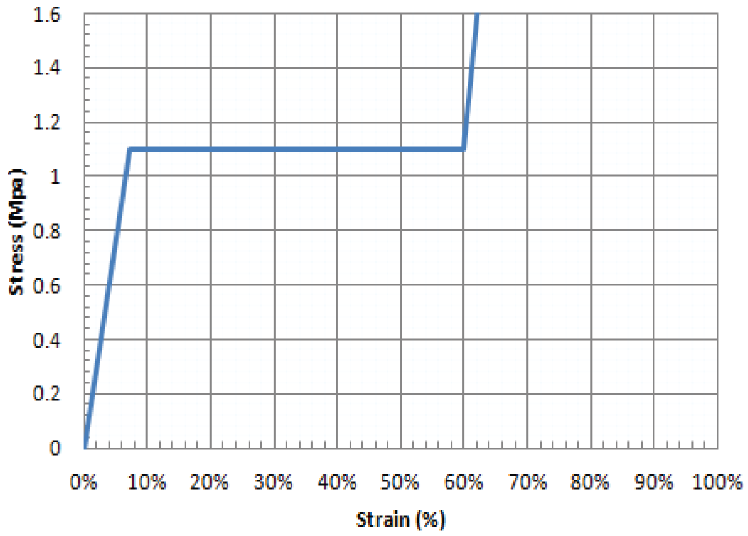

Figure 4: Foam stress/strain curve used for polyurethane foam in simulation 1

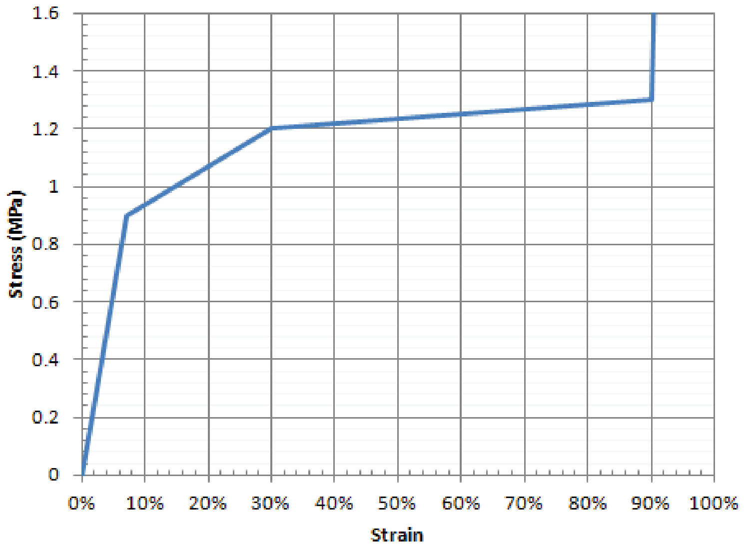

Figure 5: Foam stress/strain curve used for carbon foam in simulation

shown in Table 1 were derived from coupon tensile tests of similarly laid material. If in future orthotropic ply level properties become available, the model can quickly be adapted to incorporate this information.

Another important feature of the model is failure criterion. The composite shell element sets and CV element set have defined failure stresses. For the composite elements, an advanced composite material model is used with the Belytschko-Tsay formulation, wherein when the stress in a particular element and ply exceeds an assigned value, that particular ply in the element is removed. Once all plies in an element have exceeded the maximum stress level, the entire element is removed from the simulation. The model also has the capability to determine matrix and fiber failure independently given the proper input. For the CV elements, once an assigned compressive or tension stress is exceeded, the element will fail and be removed from the simulation.

Table 1 shows all the composite material properties used to test and validate the model. Some material properties required to fully define each structure were not found in the experimental test data report, and so engineering judgment was used in assigning values for the unknown quantities.

Table 3. Key Differences between Test 2 and Test 4b

	Impact Velocity (m/s)	Specimen Mass (Kg)	Cell Wall Thickness (mm)	Foam Composition	Maximum Crush Stroke
Test 2	30.3	9.30	2.08	Polyurethane	60%
Test 4b	40.4	14.31	4.75	Carbon	90%

Table 4. Foam, Impact Surface, and CV Material Properties

	PU Foam		Carbon Foam		Impact Surface		CV	
Material Model	063-Crushable Foam		063-Crushable Foam		020-Rigid		013-Isotropic Elastic Failure	
Modulus**	2.0E+07	Pa	2.0E+07	Pa	2.0E+11	Pa	2.69E+10	Pa*
Yield	1.1E+08	Pa	6.0E+07	Pa	n/a	-	3.44E+07	Pa
Density	85.78	kg/m^3	91.26	kg/m^3	2000	kg/m^3	383	kg/m^3
Poison's Ratio	0	-	0	-	3.00E-01	-	3.00E-01	-
Damping Coef.	0.5	n/a	0.3	n/a	n/a	-	n/a	n/a
Bulk Mod.	-	Pa	-	Pa	n/a	-	5.83E+10	Pa

*Material model 013 defines a shear modulus rather than an elastic modulus. The value shown is the shear modulus
** This value is overridden by the foam stress/strain curve previously shown

The developed model was validated against two experimental impact cases, test 2 and 4b from the Kellas report. These test cases were used because the two cases had the most information recorded about them in the report. The cell wall thicknesses shown in Table 2 are taken directly from the report. The inner and outer sphere thicknesses were indirectly calculated based on other thickness information found in the report. Efforts were made to match all reported dimensions when possible.

The two test cases modeled have significant differences. The most apparent of which were in the impact velocity, specimen mass, cell wall thickness, and crushable foam composition. Test 2 used an expanded open cell polyurethane foam, whereas Test4b used an open cell carbon foam. A summary of the key differences is found in Table 3. It is important to note that foam properties are highly rate dependent and that the true properties of each foam are not fully characterized at the high crush velocities found during an EEV earth impact. This is because at this stage it is impractical to measure the in-situ of material properties at the impact velocities ranging from 30 to 40m/s. In Ref. 4 attempts have been made to measure the strain rate dependent properties by using crush rates at high as 3.8m/s. Although the tests uncovered non-linear strain rate effects, the rates tested are not high enough to be representative of the EEV impact enviroment. Figures 5 and 6 show the stress vs. strain curves used in the simulations for each of the foams.

Other material properties for the polyurethane foam, carbon foam, impact surface, and CV are found in Table 4. Many of the material properties have little significance in how the simulation is run, however the FE code requires values for these terms and so they are

Table 5. Balanced Mass Information for Test 1 and 2

	Mass (kg)			
	Test 1	Spec. 2	Test 2	*Spec. 4b*
Cell Walls	0.811	-	1.764	-
Outer Shell	0.223	-	0.393	-
Inner Shell	0.118	-	0.072	-
PE Foam	1.157	-	1.144	-
CV	0.190	0.189	0.177	0.189
OS	0.293	3.65	0.279	3.65
Impact Sphere Total	2.498	1.279	3.828	1.914
Mass Elements	6.531	-	10.482	-
Model Total	9.32	9.30	14.31	14.31

presented here. One value in particular that is of interest is the elastic modulus term for the crushable foams. The 063 material model requires a stress strain curve such as those found in Figs. 4 and 5. To be as rigorous as possible, the curves as well as the modulus values found in Table 4 were matched directly from previous data from Ref. 4. The slope of the curves in the figures are significantly different than the values in the table. When running simulations the solver outputs a warning about this discrepancy but the results of the simulation are not affected. The solver uses the slope from the curve.

Lastly and before moving on to the results of the impact testing, in order to match the test cases, the masses needed to be set equal to each other. The impact spheres that were impact tested at NASA are different than the developed model in that the tested spheres were hemispherical and had heavy data acquisition equipment attached to them. It is not expected that the hemispherical shape would cause significant differences in crush results because the crush zone is well within the lower half of the hemisphere. However, the extra mass of each test rig needs to be accounted for. This was done by adding mass elements to the model. A total of 3576 mass elements were added to the OS surface in the model. One mass element was added at each node on the OS. And, a mass balance was conducted. A summary of the mass balancing procedure is found in Table 5. The test 2 model matches the 9.3Kg mass of specimen 2 and the test 4b model matches the 14.31Kg mass of specimen 4b. Notice that the mass of the IS model is double that of the test specimens due to their hemispherical rather than full spherical shape.

Impact Model Results

For the impact model, results are presented in three sections. First, the damping parameter setting was investigated to determine its effects on the EEV crush response. Then, an impact orientation study was conducted, where the impact sphere was impacted perpendicular to the rigid surface but with various parts of the IS impacting the surface first. Lastly, the model was validated against two experimental test cases conducted at NASA Langley Research Center (LaRC) in 2002.

Damping Parameter Study

It was found early in the project that the 063 crushable foam material model has an adjustable damping parameter. The code manual describes this parameter as "rate sensitivity via damping coefficient" Because the various foams in the IS are all rate sensitive, an investigation of this parameter was deemed warranted.

For this study, the IS was oriented so that a cell wall edge was the first point of contact with the rigid surface. This study is intended primarily as a qualitative study to uncover the effects of the damping parameter and as such material property details have not been included. The simulation was run for six different cases, setting the damping parameter beginning at 0.0 and increasing in 0.1 intervals up to 0.5. The change in the impact response was evaluated by observing the diplacement, velocity, and acceleration time response during the impact. Figures 7, 8, and 9 show the displacement, velocity, and acceleration time histories for the OS, respectively. Rate sensitive foams have been shown to stiffer material properties during high speed crushing and exhibit an exponentially

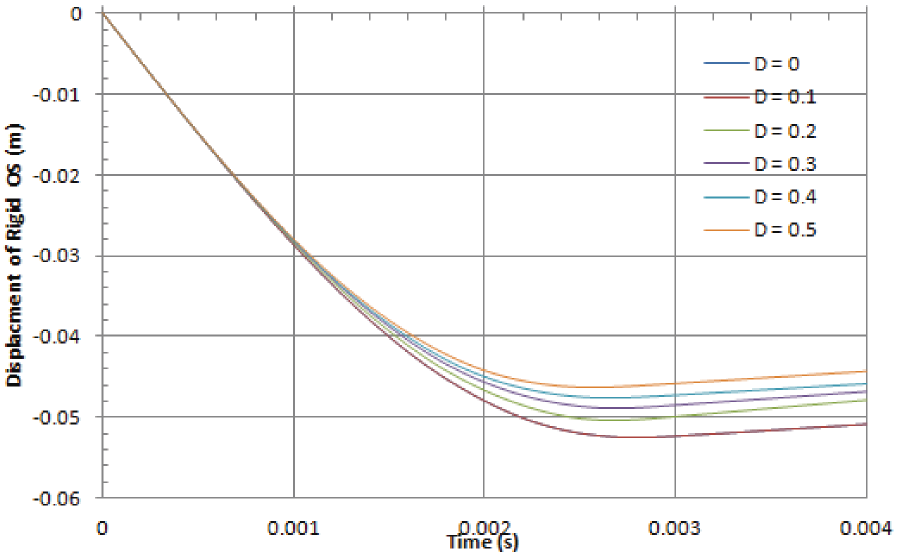

Figure 6: Comparison of OS displacement for 6 different damping parameters

stiffer response as the crush stroke becomes large[4][7]. In many foams, particularly the carbon foam, at low strain rates the exponential stiffening is not observed[4]. Thus when evaluating the FE code's damping parameter, a structural stiffening effect was expected. First the displacement date in Fig. 7 will be discussed.

Compared to the zero damping parameter peak OS displacement was reduced by about 15% when using the 0.5 damping parameter. Also of note is that the peak displacement occurred as much as 0.3ms earlier for the 0.5 damping parameter case. Based on Fig. 8, it can be seen that the IS reaches the zero velocity point about 0.3ms earlier for the 0.5 damping case than for the 0.0 damping case. However, the final rebound velocity remains relatively unchanged regardless of the damping. This is a good indicator that the damping parameter does not alter energy absorption by the IS during impact.

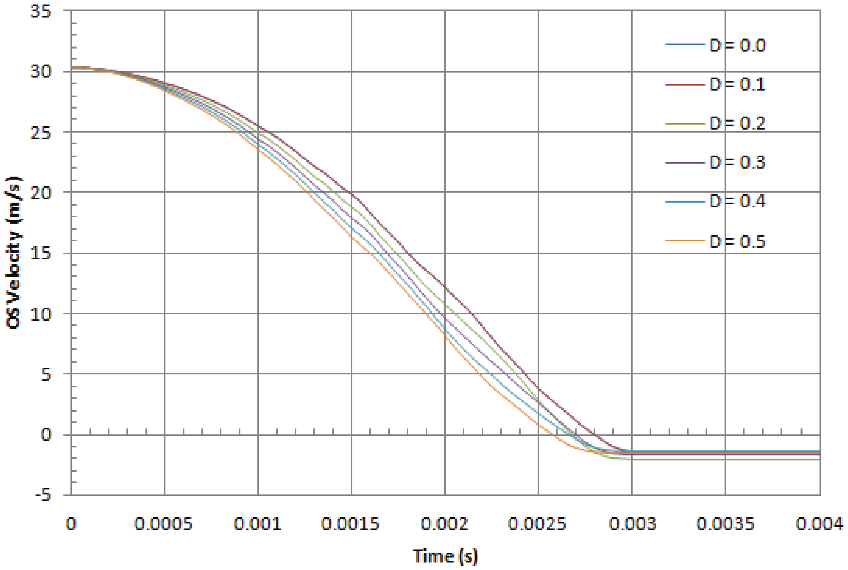

Figure 7: Comparison of OS velocity for 6 different damping parameters

The acceleration time history plot in Fig. 9 shows an interesting and complex damping effect. Higher damping coefficients significantly steepen the rise of the acceleration curve during the first 2ms of the impact. Despite the steeper curve, the peak acceleration of the higher damping coefficient cases is only slightly higher than that of the 0.0 damping coefficient case. This peak acceleration occurs about 0.3ms earlier than those for the lower damping coefficient cases. The total acceleration pulse is about 0.2ms shorter for the 0.5 damping coefficient case than for the 0.0 damping coefficient case.

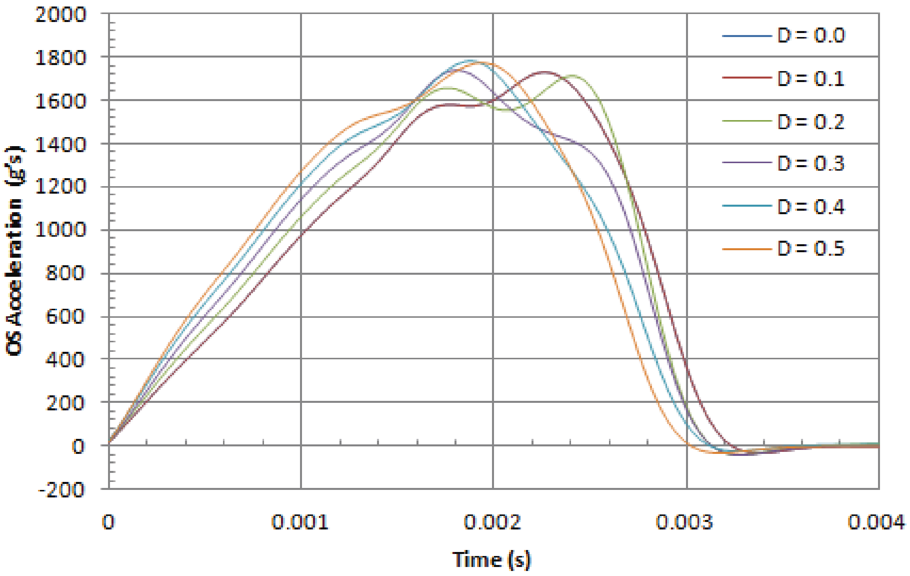

Figure 8: Comparison of OS velocity for 6 different damping parameters

The damping parameter study uncovered three important points. First, an inverse relationship between damping coefficient and peak displacement was observed with about 15% lower peak displacement for the high damping parameter case. Secondly high damping coefficients shorten the acceleration pulse but have little effect on total energy and final rebound velocity. And lastly, the acceleration curve becomes significantly steeper and occurs earlier with larger damping parameters but peak acceleration rises only slightly (less than 5%).

Impact Orientation Study

The impact sphere is composed of pentagonal and hexagonal shaped foam cells each wrapped with carbon fiber and Kevlar material. Due to this special and non-uniform structure, the impact response of the IS was presumed to be different for a range of impact orientations. The impact orientation study examined four different impact orientations. Impact orientations have been named by the area of the IS that would first contact the rigid surface during an impact. The chosen orientations are hexagon cell center, pentagon cell center, cell wall edge (the cell wall edge between a hexagon and pentagon cell), and Y intersection (the point where three cell walls merge). The resulting displacement, velocity, and acceleration data at the OS were then compared.

This study uses material properties and dimensions comparable to the NASA specimen 2 as mentioned in the impact model description section. Displacement curves for all four impact orientations and the NASA test 2 data are shown in Fig. 10. In the figure, the red line is the NASA curve which can be seen to cut off at about 2.8ms. The cutoff is due to the test specimen experiencing damage to its data recorder during the impact, preventing data

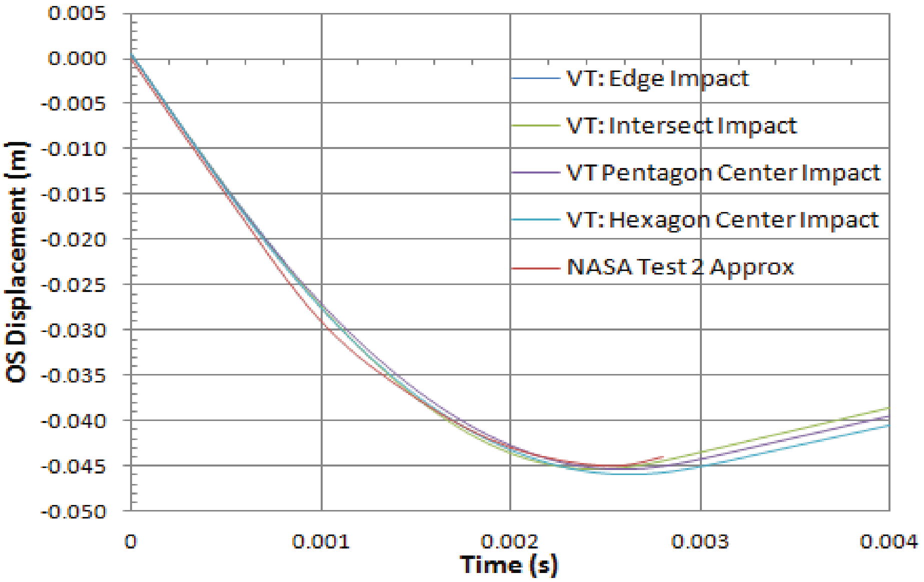

Figure 9: OS displacement comparison for various impact orientations

collection past 2.8ms. The peak displacement (which is analogous to maximum crush stroke) for all cases is between 45mm and 46mm. This narrow range of peak displacements indicates that there is little correlation between impact orientation and peak displacement. Velocity curves for all four impact orientations and the NASA test 2 data are shown in Fig. 11. Several differences and similarities were observed in the velocity curves. First, the curves for the edge orientation and Y-intersection orientation have a very similar shape and are slightly steeper than the curves of the cell center orientations. Secondly, the rebound velocity is reached approximately 0.3ms earlier for the edge and Y-intersection

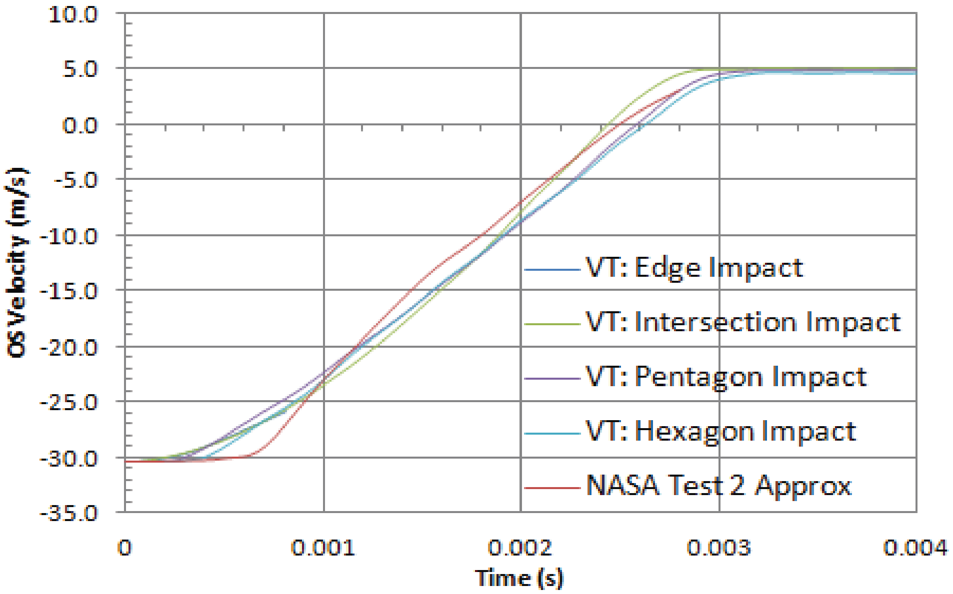

Figure 10: OS velocity comparison for various impact orientations

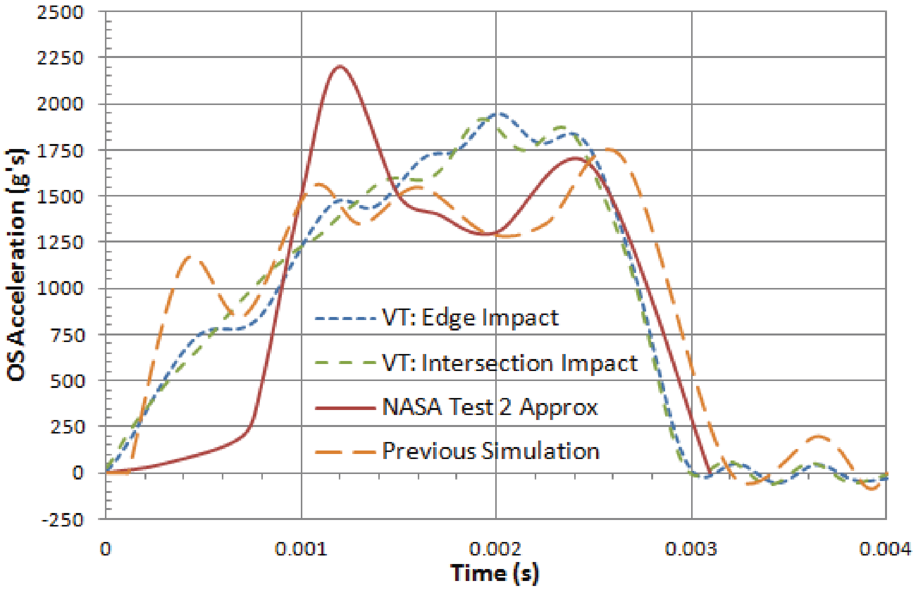

Figure 11: OS acceleration comparison for edge and Y-intersection impact orientations

orientations than for the other orientations. And lastly, the final rebound velocity of 5m/s is nearly the same for all four impact orientation simulations, which is a good indicator that the same amount of energy is absorbed by the IS regardless of impact orientation. Although the test data was lost before reaching the final rebound velocity, by visually extrapolating the curve one could expect the final rebound velocity of the test specimen to be close to 5m/s.

The acceleration curve data was divited into two plots for added clarity. Figure 12 presents four accelerations curves. The first curve shown in solid red is the NASA test 2

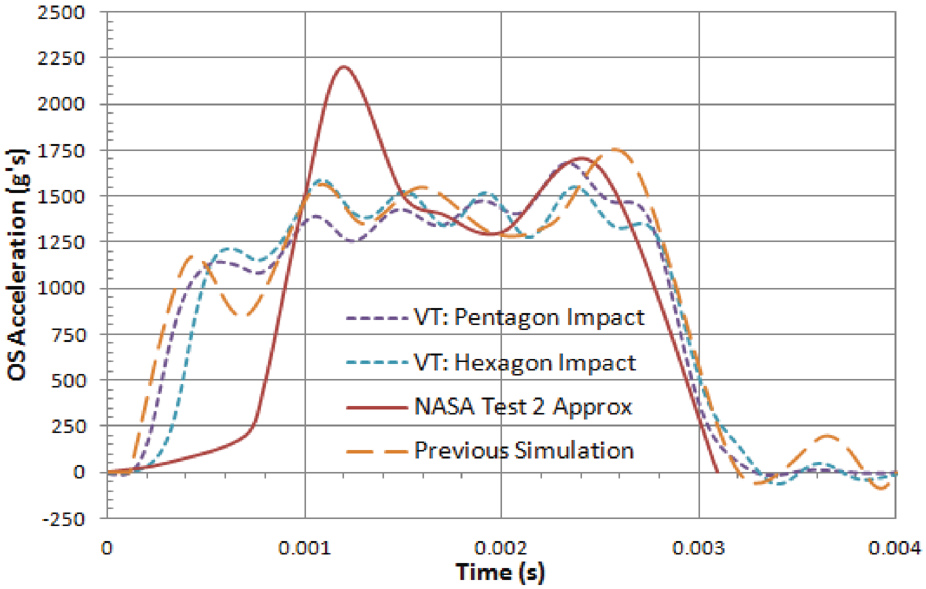

Figure 12: OS acceleration comparison for pentagon center and hexagon center impact orientations

data, the second curve shown in long-dash orange is the data from Ref. 6, the third line shown in short-dashed blue is the edge orientation simulation, the fourth curve shown in short-dashed green is the Y-intersection simulation. Figure 13 presents the NASA data and the test 2 simulation data from Ref. 6 in the same manner but the edge orientation and Y-intersection orientation curves are removed and replaced with the pentagon center curve shown in short-dashed purple and the hexagon center curve in short-dashed blue.

The first thing to notice is the significant difference in curve shape between the simulation data and the test 2 accelerometer data. The NASA data shows a sharp peak at 1.2ms not found in the simulation curves. This has been discussed in Refs. 4 and 6. The likely cause for this early peak can be due to the existence of a narrow gap between the OS and IS. Initially, the small gap results in low measured accelerations for the first 0.8ms of contact because the OS and IS are essentially two separate bodies. The IS, already in contact with the rigid surface slows down quicker than the OS. Once the gap between the IS and OS is closed, the velocity of each sub-body is forced to equalize, resulting in the acceleration spike. When comparing the data found in Figs. 11 and 12, significant differences between the cell wall orientation curves and the cell center orientation curves are observed. The cell wall edge cases appear to have a more severe acceleration response with higher peak accelerations. Peak acceleration for the cell wall cases occurs a full 0.5ms earlier and is 300g's higher than for the cell center cases. The difference between the two is about 20%. Also, both cell center orientation curves follow a very similar path to the curve found in the Ref. 6 simulation. Looking again at the NASA test 2 curve, if one were to neglect the initial sharp peak (due to the small gap as explained), the test 2 data appears to have a similar response where both simulations and test 2 have a peak at about 2.5ms with similar severity of 1750g's. The similarity of the curves found in Fig. 13 is indicative that hexagon center is likely the orientation in which impact occurred experimentally in Ref. 4 and through simulation in Ref. 6.

In summary, the impact orientation study determined three important points. First, the impact orientation has little effect on OS diplacement or crush stroke. This is useful in that maximum crush stroke is a common impact performance metric. Second, final rebound velocity is unaffected by impact orientation, stressing that the same amount of energy is absorbed by the IS in all cases. Lastly and most importantly, peak accelerations for the cell wall edge orientation and Y-intersect orientation cases generated the highest peak acceleration in the OS. The peak accelerations for these cases was 300g's and about 20% higher than those found in the lowest peak acceleration case, the hexagon center case. This is important because the purpose of the impact sphere is to minimize peak acceleration at the OS.

Impact Model Validation

The EEV impact simulation is extremely non-linear with huge element distortions and inversions occurring due to the impact event. By adjusting the solver settings, relevant instability problems were adequately addressed: Using the default settings, the first model design showed very good correlation with test results. Changing the material model from a basic composite material model to an enhanced composite model with damage, and changing the composite failure theory to Belytschko-Tsay, improved simulation stability and results. Furthermore, modifying the solver settings so that highly distorted and inverted elements were deleted solved several stability problems incurred during early stages of model development.

To confirm that the model could be quickly modified parametrically as well as to ensure that the model could be validated against multiple test cases, model parameters were quickly modified to match the test 4b geometry and material properties. As shown in more detail later in this section, the developed model was effectively validated against the available test data using two test cases, Test 2 and Test 4b.

Test 2 Validation

For the test 2 model validation displacement, velocity, acceleration, energy, and qualitative images were evaluated. As a note, in Figs. 13 to 20 the NASA data and previous simulation data are labeled "Approx" because this data was extracted visually from the two reports. After manual extraction from the reports, the data was input together with the developed simulation output data into the plotting software[4][6].

Figure 14 shows the OS displacement plot for specimen 2, the Ref. 6 simulation, and the developed model. All displacement curves show very good agreement with each other. The developed model displacement prediction is slightly more conservative, predicting peak displacement to be 1mm more than the other simulation and experimental results. In Fig. 15, the developed model velocity curve shows good agreement with the test results with the exception of the area between 0ms and 1m/s. This initial discrepancy between the simulation data and experimental data is likely due to the gap between the OS

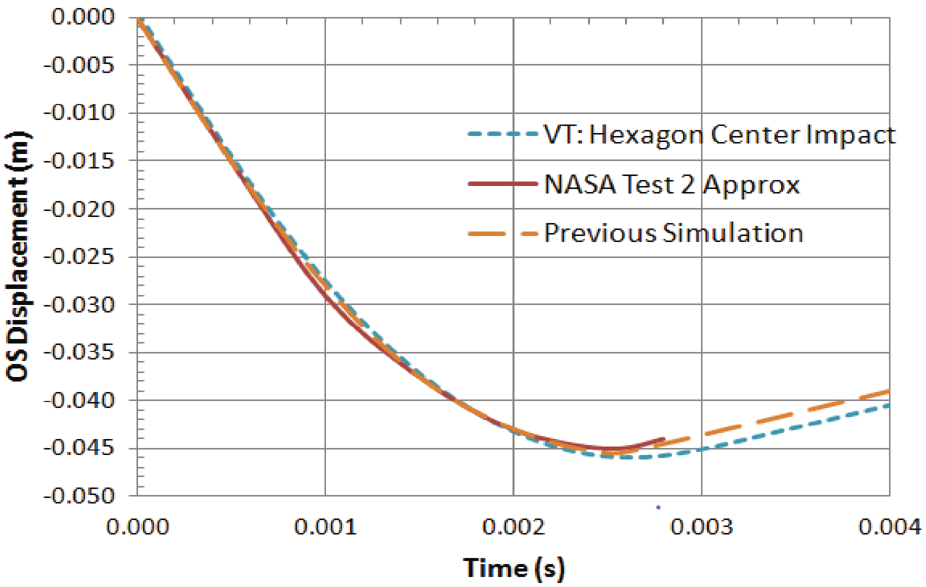

Figure 13: OS displacement plot for specimen 2 and simulations

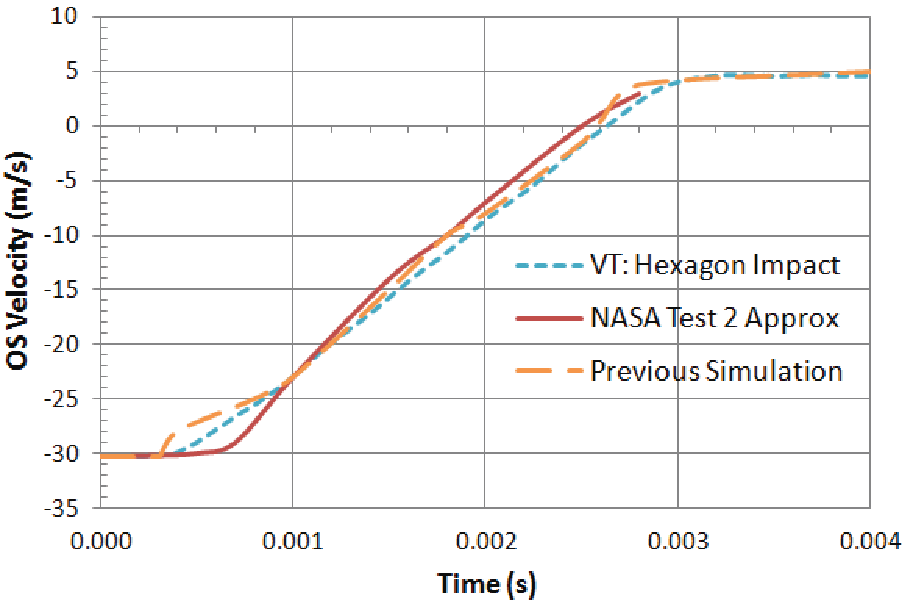

Figure 14: OS velocity plot for specimen 2 and simulations

Explicit FE simulations with very large deformations demonstrate the propensity to experience high energy losses due to hourglassing and other issues. Such energy losses can indicate poor simulation accuracy and so an investigation into the model's energy balance was conducted. A plot of the results is found in Fig. 17. In the figure kinetic energy, internal energy, total energy and hourglass energy are plotted. The simulation begins with 4300J of pure kinetic energy, almost immediately due to the impact and deformation; the kinetic energy is converted into internal deformation energy as the EEV slows down. After 2.3ms the IS has reached zero velocity and internal energy is at its peak of about 4050J.

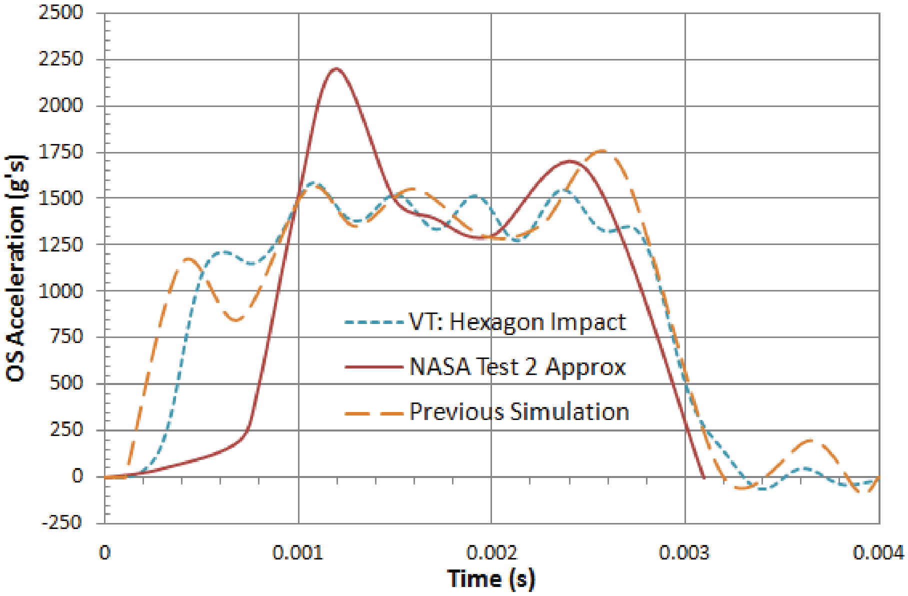

Figure 15: OS acceleration plot for specimen 2 and simulations

The difference between the initial kinetic energy and the final internal energy is the hourglass energy loss which is about 250J. Next between 2.3ms and 2.9ms the IS exhibits a partial elastic recovery and converts about 200J back into kinetic energy as the IS rebounds off the rigid surface at 5m/s. About 6% of total energy was converted into hourglass energy, which is below the 10%, level considered acceptable by many FE analysts. The results of the energy study provide a good second confirmation that the model is outputting acceptable data.

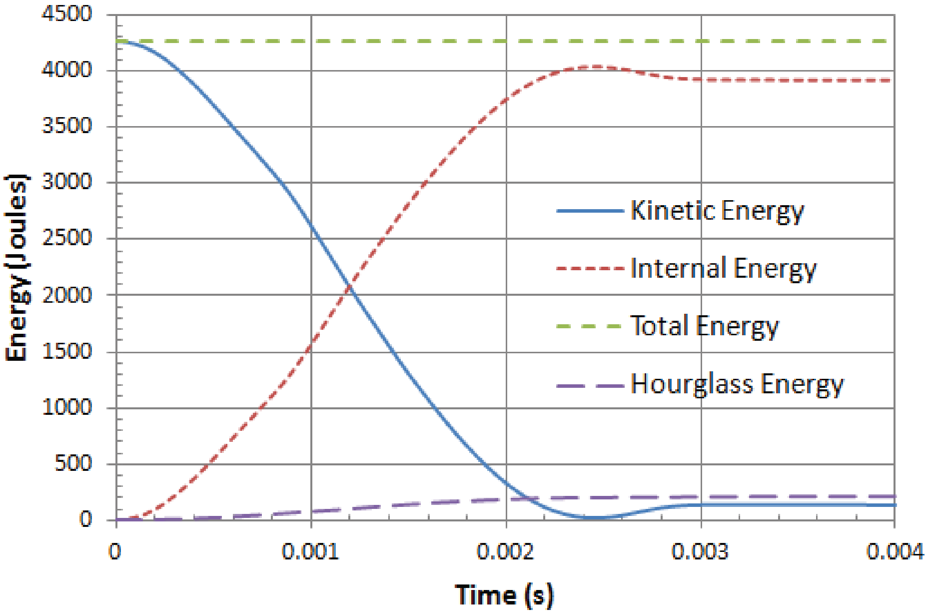

Figure 16: IS energy plot for test 2 simulation

In addition to the quantitative validation conducted on the developed model, a qualitative comparison was conducted to see how well the model could capture the more general failure behavior, particularly of the cell walls. Figure 18 shows three images of the crushed IS structure. The first image is a cross section of the test 2 model after impact with the crushed foam elements visible, the second image is a picture from Ref. 4 of the test 2 sphere after impact, cut in half, exposing the impact area, and the third image is the same image as the first but with the foam elements hidden from view so that the cell wall elements can be better seen. Comparing the first and second images in the figure, it can be seen that both the simulation and test images show similar crush strokes and foam crush behavior. Both images show that the foam crushes and moves outward and away from the central impact area. Comparing the second and third images in the figure the failure behavior of the cell walls can be evaluated. In the image below the dotted line the cell walls buckle and bend locally (crimpling). The cell walls do not fracture and they remain connected with the outer shell. Also, notice that above the dotted crush line the cell walls still appear straight, almost unaffected by the impact and crush behavior below the line. This same failure behavior can be seen in the third image where localized buckling is widespread in the crushed area, but above the crush zone the cell walls look unaffected.

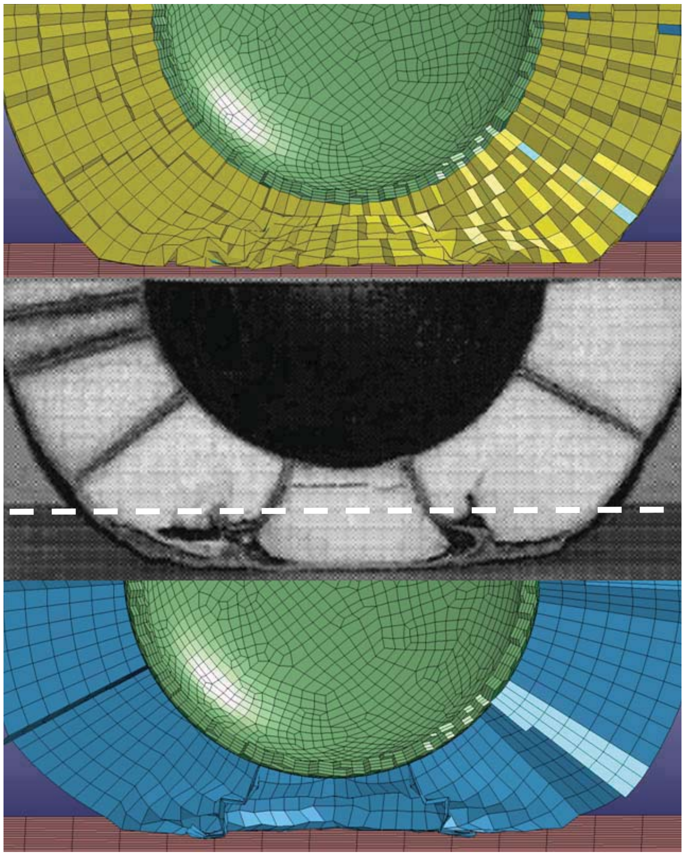

Figure 17: Qualitative comparison of crush zone for test 2 simulation

Test 4b Validation

In order to validate the model against specimen 4b several changes needed to be made to the model. First, although the geometries were very similar, a scaling process was completed so that the model would closely match the new dimensions. Next shell element thicknesses, layups, material properties, initial velocity, and total mass were adjusted to match specimen 4b specs as described in the model design section. For the test 4b model validation displacement, velocity, acceleration, and qualitative images were evaluated.

In Fig. 19 the OS displacement plots are shown for specimen 4b and simulations. The developed model has a peak displacement of 55.3mm, the previous simulation crushes 54mm, and the experimental test had the highest displacement of 57mm. The developed model has a slightly steeper displacement curve and reaches its peak acceleration 0.3ms earlier than specimen 4b. Both simulations underestimate the crush stroke and reach the maximum crush stroke prematurely compared to the experimental results. The developed model is however a significant improvement over the previous simulation results. The Kellas report indicates that there was some instrumentation issues and even possibly some carbon foam defects that could have altered the experimental results. This is particularly true when examining the acceleration time history plots in Fig. 21.

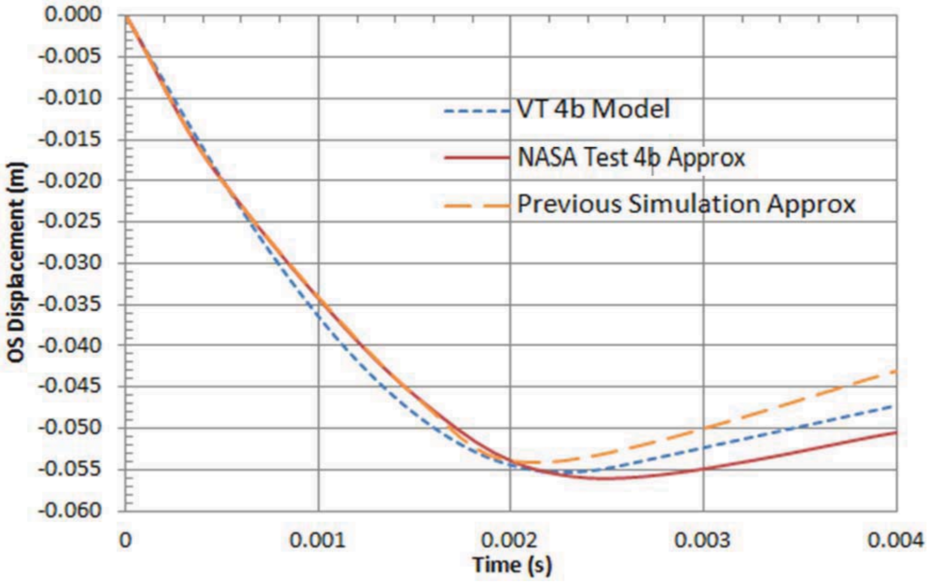

Figure 18: OS displacement plot for specimen 4b and simulations

The OS velocity curves for the 4b specimen and simulations are compared in Fig. 20. Initially the experimental curve and previous simulation curve follow very closely. However, after about 1ms into the impact the previous simulation curve rises above the experimental curve and then has some peculiar vibrations during the rebound portion of the plot. The final rebound velocity of the developed model and the experimental test are nearly identical at 4m/s. Overall, is can be seen that the test 2 velocity data and developed model velocity data show good agreement.

The OS acceleration data found in Fig. 21 is difficult to interpret because damage to the internal data acquisition equipment occurred at about 2.2ms into the impact[4]. This damage likely caused some of the sharp and erratic spikes in the data beyond this time. To deal with this problem both Kellas and Billings use an averaging technique to smooth out the data and remove some of the sharp peaks. Different data referring to the same experiment was found in the Kellas and Billings reports, so it was decided to plot one average acceleration curve from each report. The method in which the data was averaged can be found in their respective reports. Depending on which curve is used the developed model predicts between 300g's under or 100g's over the experimental data. The developed model predicts a shorter and flatter curve than the experimental data. Depending on the data referenced the developed model's acceleration pulse ends earlier than the experimental data by 0.5ms to 1.0ms. Although not in perfect agreement with the experimental data, the developed model captures all the major trends of the impact event. Some possible reasons for the discrepancies include: problems with the accelerometers as mentioned previously, poorly characterized high strain rate foam properties, damaged foam that was reported could have caused excessive crush and a bottoming out of the structure, and a different impact orientation than that was modeled. The author suspects that all of the above reasons likely have played a part in the discrepancy.

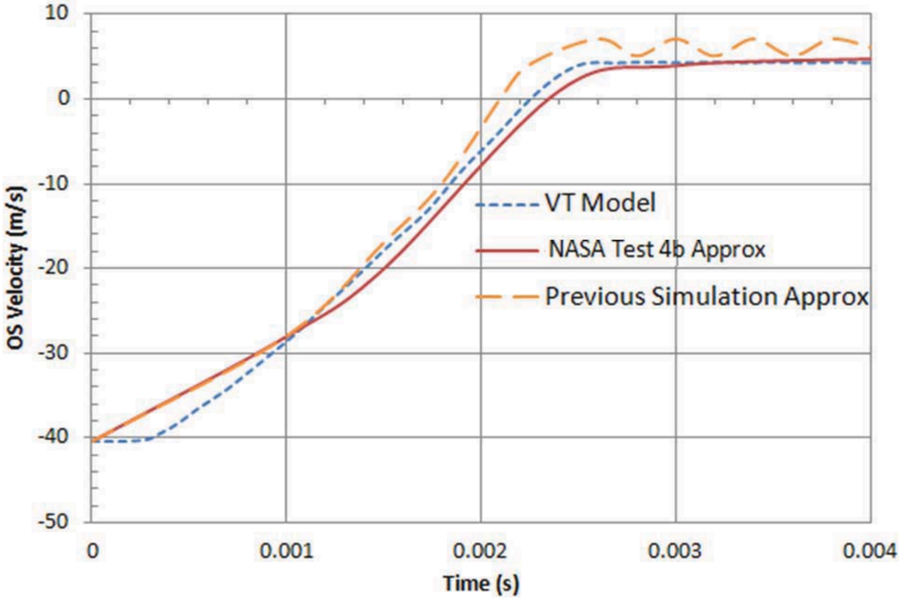

Figure 19: OS velocity plot for specimen 4b and simulations

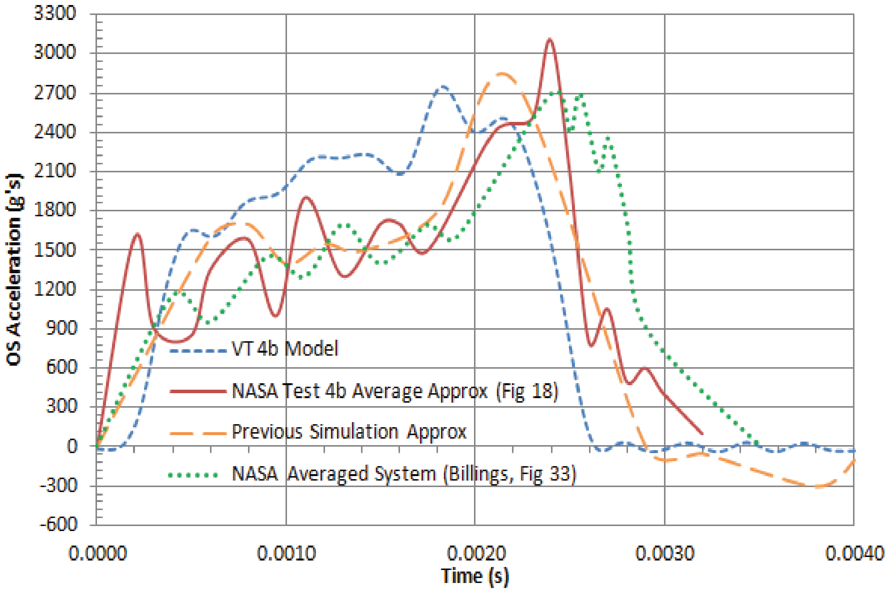

Figure 20: OS acceleration plot for specimen 4b and simulations

Again for the test 4b specimen a qualitative comparison was conducted to see how well the model could capture the more general failure behavior, particularly of the cell walls. Figure 22 shows three images of the crushed IS structure. The first image is a cross section of the test 4b model after impact and with the crushed foam elements visible, the second image is a picture from the Kellas report showing the test 4b sphere after impact, cut in half with the

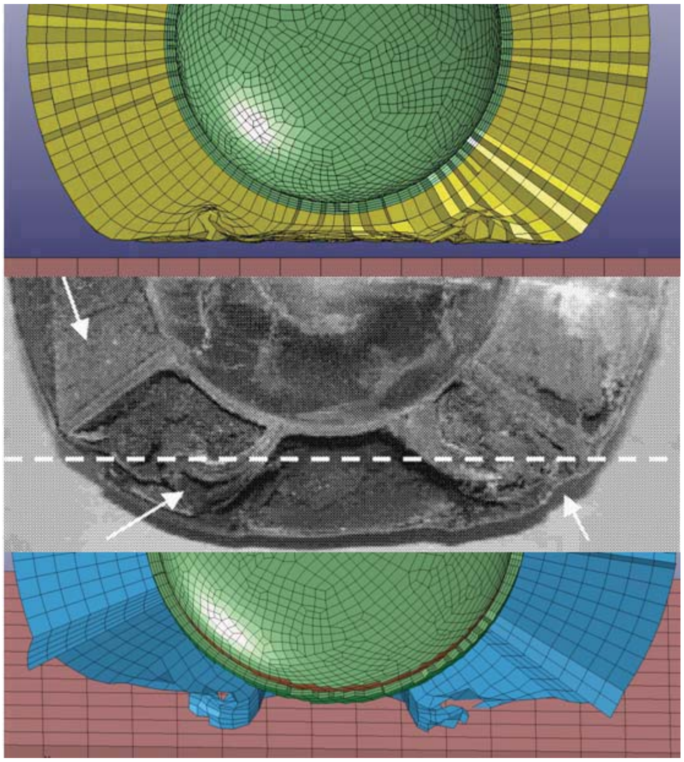

Figure 21: Qualitative comparison of crush zone for test 4b simulation

impact area exposed, and the third image is the same image as the first but with the foam hidden from view so the cell wall elements can be seen more easily. Comparing the first and second images in the figure, it can be seen that both the simulation and impact test show similarly deep crush strokes and foam crush behavior where the foam crushes and moves outward and away from the central impact area. Comparing the second and third images in the figure the failure mechanism of the cell walls can be evaluated. In the images notice that unlike the test 2 case, in this case, below the dotted line the cell walls flare outward and become disconnected from the outer shell. This same failure behavior can be seen in the third image which shows the cell walls broken away from the outer shell and flared away from the impact zone.

Structural Dynamics Model Design

The purpose of the structural dynamics model (SDM) is to evaluate the structural response of the EEV during the launch and reentry portions of the EEV mission. The SDM was build in the implicit FE solver Patran using Patran Command Language (PCL). Building a complicated model using PCL can take much longer but once the model is built, unprecedented parameterization and automation of nearly all simulation processes is possible. This allows the engineer to quickly build, run, and analyze a broad spectrum of possible EEV designs. The developed model has the advantage of saving the engineer large amounts of time in the long run and allowing a design trade space to be uncovered that without a parametric model would be much more difficult to uncover.

The SDM model was constructed, parameterized, and automated through the writing of over 3000 lines of PCL code. The code has been parameterized for rapid changes to the following areas: geometry, material properties, loading, boundary conditions (BC), mesh settings, and analysis settings. The parameters can easily be changed directly in any readily available text editor, or to automate a broad array of simulations, a 3rd party code as proposed by Samareh et al. can also be implemented[3].

At this point in time a full EEV prototype has not been constructed for structural dynamics testing. Thus experimental validation of the SDM is not currently possible. Unlike in the impact model that focused strongly on results and validation this section will focus more on the parametric capabilities of the model and the results will show how effective the developed model can be used as a design tool for NASA engineers. With that in mind it should be understood that material properties, composite layups, dimensions, etc. are presented only as reference quantities used to show the model's capabilities.

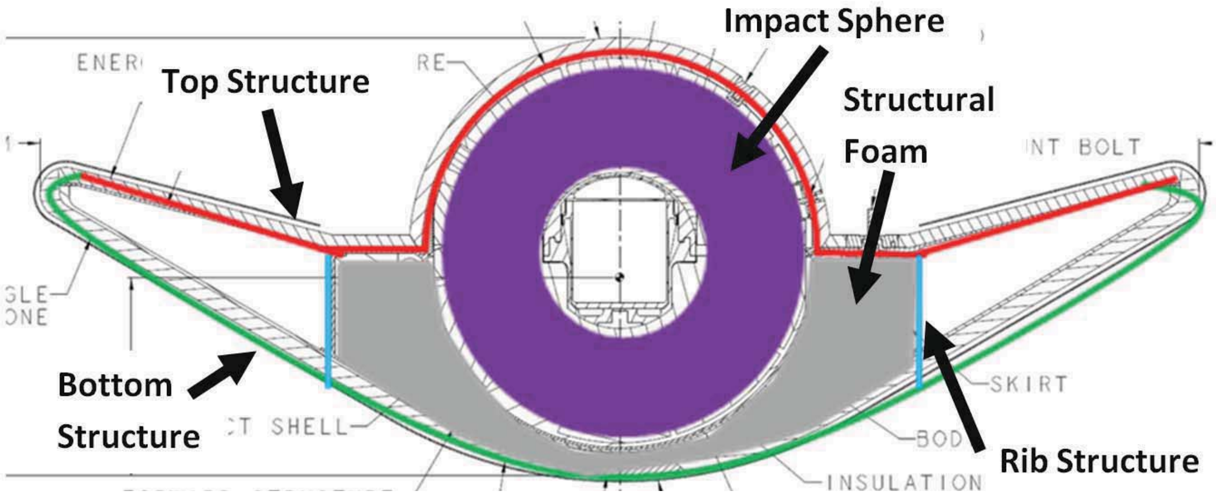

Figure 22: EEV structure divided into 5 sub-sections

In the impact model the primary structure and TPS were determined to have a negligible effect on the simulation response and therefore were not modeled. For the SDM however these structures compose the primary area of interest and therefore must be included in the simulation. The SDM has been built by subdividing the EEV into five sub sections. For easy identification of each sub section an engineering drawing of the MSR EEV concept overlaid with the color coded sub-sections is presented in Fig. 23. The five sub sections visible in the figure are the top structure (red), bottom structure (green), rib structure (blue) , structural foam (grey), and IS (purple).

Each sub-section uses a different element and material model. The top structure, bottom structure, and rib structures are all constructed of quad4 type shell elements and have been assigned a composite material model. Each group can have ply level properties and layup directions assigned independently. For model testing each structures was assigned 8 plies and typical quasi-isotropic carbon-fiber epoxy fabric properties ($E_{11,22}$ = 70 GPa)[9]. The top structure was assigned a total thickness of 8mm, the bottom structure was assigned a thickness of 16mm, and the rib structure was assigned a thickness of 12mm. To account for the added TPS mass without unnecessarily complicating the model, both the top and bottom structures were assigned different values of non-structural mass. The top structure was assigned a value of 2.56kg/m^2 which corresponds to SLA-561V and the bottom structure was assigned a value of 29kg/m^2 which corresponds to carbon phenolic[10]. The structural foam elements were constructed from hex8 solid elements with a linear isotropic material model. The material properties used for the structural foam are Rohacell 110 WF which has a density of 110kg/m^3 and an elastic modulus of 180MPa[11]. Lastly, the IS has material properties consistent to those used in the test 2 validation case.

Parametric Model Build Features

Several parametric model build features have been incorporated into the model that enable to model to be built and run automatically without any required analyst interaction. The three key features that will be discussed are: the model's geometric variations and automated meshing capability, the method of attaching the imported IS to the EEV, and the way boundary conditions are assigned.

Geometric Variation and Automatic Meshing

Seven geometric parameters have been built into the model which allow the model to take on nearly any dimensionally possible "EEV like" shape. That is to say lines can be lengthened and shortened and radii can be made larger or smaller, but new features cannot be created and existing features cannot be removed. The seven geometric parameters are shown in Fig. 24 and are listed with their base configuration dimension. A few extreme geometries were built and are presented in Fig. 25 to show the reader what the developed

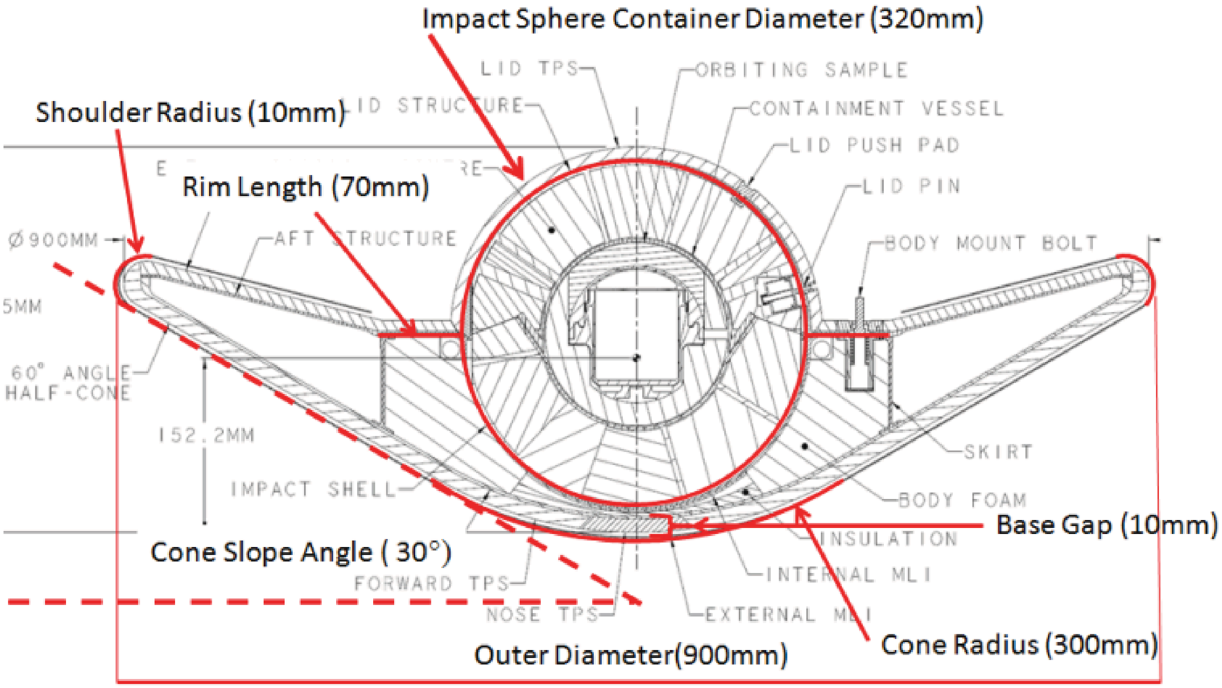

Figure 23: The seven geometric parameters and their base configuration dimensions

design tool can quickly do, simply by changing different dimensional parameters. Also, the meshing of the model is automated, and mesh density can be varied by a single parameter or through the combination of sub parameters. The result of automatic meshing can also be seen in Fig. 25.

Automatic Importation and Attachment of the IS

The impact sphere is attached to the EEV primary structure using a set of cbush elements. Cbush elements are 1D combined spring and damper elements that connect two nodes together and are assigned stiffness and damping values. The cbush elements used to test the model were assigned axial stiffness values similar to that of a short 3/8" steel bolt and zero damping. The IS was converted into Patran format and all model settings and material properties were checked and adjusted to ensure proper function in the Patran environment. Once a suitable Patran compatible IS model was developed, Its importation into the EEV model was automated in the developed PCL code.

The IS is connected to the EEV in two regions, the first around the inner circumference of the rim as labeled in Fig. 24 and secondly in a small region at the base of the EEV. The primary challenge in connecting the IS to the EEV is that the connection process needs to be automatic and work for any mesh density and geometric variation. To solve this problem a special PCL module was written and incorporated into the code that connects

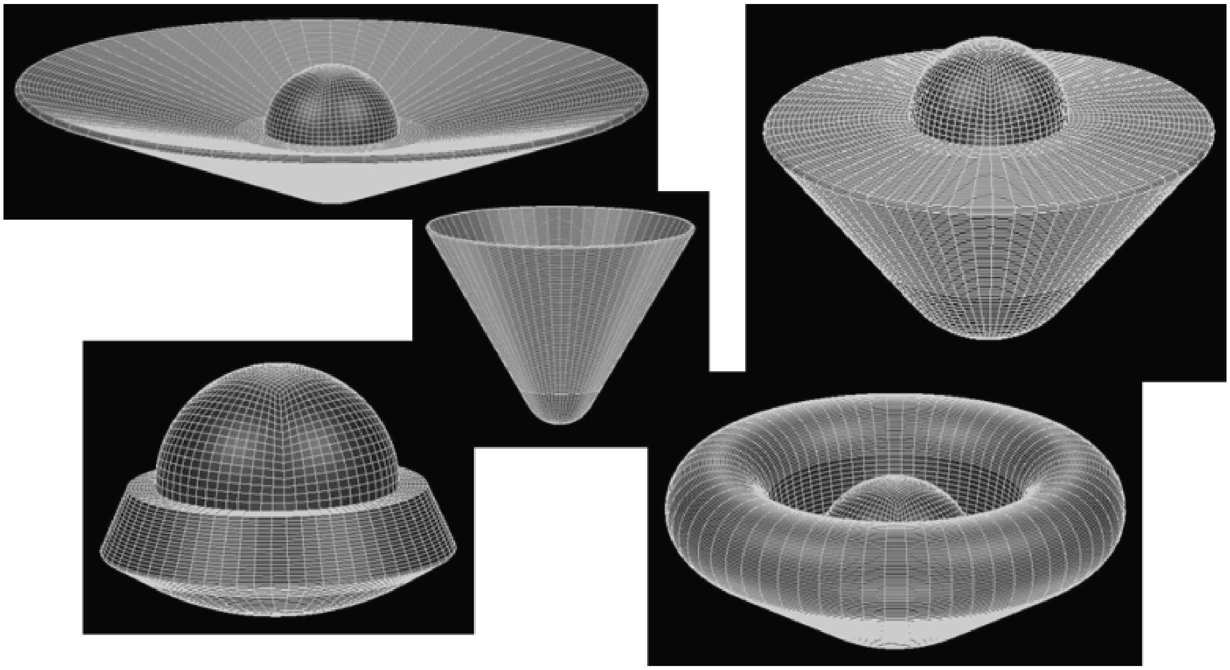

Figure 24: A selection of very different EEV geometries that can be built using the developed code

every node along the inner circumference of the EEV rim and every node inside a small region at the base of the EEV to a nearby node on the IS. The module rigidly joins the IS to the EEV primary structure and works regardless of mesh density and geometric variation.

Assignment of Boundary Conditions

The EEV will be launched into space aboard an Atlas or Delta rocket, attached to a large internal structure within the rocket. As discussed previously the EEV is remainded attached to a satelite structure that orbits the earth until the EEV is ready to return the earth. A preliminary design for this orbitiing satelite and the location in which the EEV is expected to be attached is found in Fig. 26 from Ref. 16. The EEV is anchored at three locations equally spaced from each other on the rim area of the top structure. Consulting with NASA engineers, it was decided that a minimally constrained set of BCs would be desirable in that it would minimize the number of possible stress paths through the structure. This removes the redundancy from the dynamic analysis, rendering the results more reliable. During the launch, the EEV will be oriented such that the top and bottom structures are facing perpendicular to the launch direction as shown in Fig. 27. In the figure, the approximate area of each attachment point is indicated by the three red dots. The requirement for minimally constrained BC's and the orientation of the EEV during launch resulted in three different sets of BC's for each attachment area as shown in Fig. 27. The restrained degree of freedoms are indicated in the figure by green arrows next to the red dots. The attachment point located at the highest point with respect to the launch

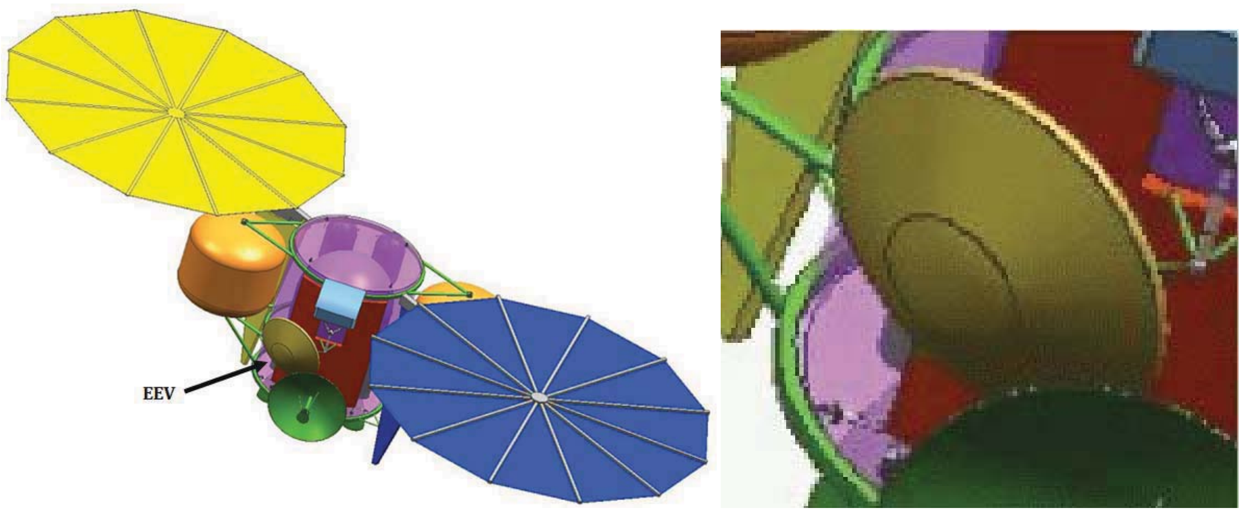

Figure 25: Location of EEV on orbiting satellite with close-up image[16]

orientation has X, Y, and Z translational degrees of freedom constrained. One of the other two attachment points has X and Y degrees of freedom constrained. The last remaining attachment point has only the Y degree of freedom constrained as shown relative to the coordinate system shown in the figure. This BC configuration has been tested and proven to generate rigid body motion in all directions.

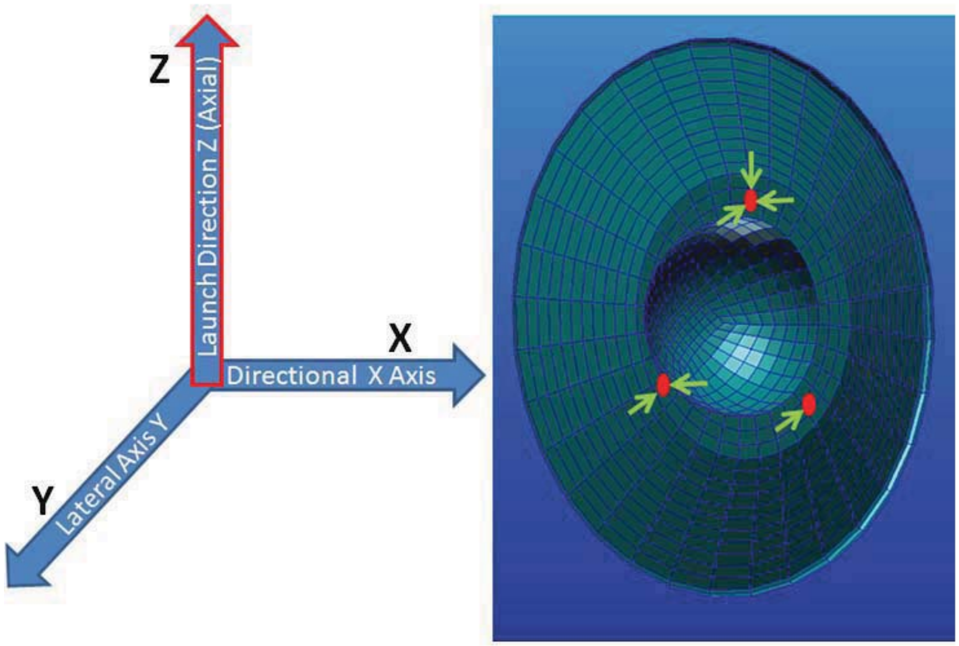

Figure 26: EEV launch orientation and minimally constrained BCs at the three attachment points

In order to correctly and automatically assign boundary conditions to the model regardless of mesh density and geometric variation, a specialized PCL module was developed. Figure 28 shows how the boundary conditions are assigned for a medium mesh density model. The module works by finding nodes in parametrically defined regions. All the nodes that are found in the region are then assigned the specified boundary condition. The module has been fine tuned so that only one radial set of nodes will ever be selected and assigned as boundary conditions. Also the mesh settings have been set so that at the minimal setting no less than two nodes will be assigned at each attachment area. These code refinements were implemented to ensure the same type of BCs are present in the model regardless of mesh density. This is an important feature for dynamic vibration analysis.

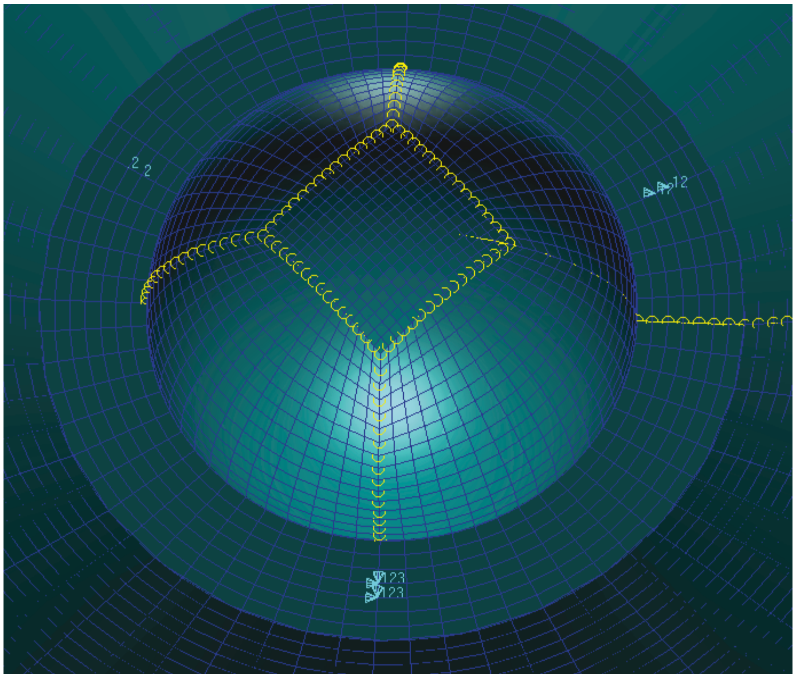

Figure 27: Example of EEV attachment area boundary condition assignment using a medium mesh density

Analysis Coding and Implementation

The SDM is intended to be used as a design tool for evaluating the system dynamic response of the EEV during the launch and reentry portions of the mission[2]. To evaluate the response the required analyses have been sub divided into four groups: quasi-static launch loading, structure born vibration frequency response, random acoustic, and reentry inertial loading. The preliminary settings for each analysis are now presented.

Quasi-Static Launch Loading Analysis

The quasi-static analysis is intended to evaluate the structural response of the EEV due to inertial loads induced during launch. In a real EEV launch, the EEV is positioned and attached to the launch vehicle by the three attachment points. Thus, for this analysis, the previously described boundary conditions are used. An inertial loading envelope for one potential launch vehicle was provided by NASA. This envelope is presented in Fig. 29 and shows all the possible combinations of axial (launch direction) and lateral (orthogonal to launch direction) inertial loads. Using the provided launch envelope, a list of inertial load cases were developed. The load envelope in Fig. 29 has been overlaid with load case information developed by the author. Taking the provided information, five points (numbered in the figure) on the perimeter of the envelope were identified as potential "worst case" load conditions. The lateral direction inertial vectors can have a positive or negative value so the five identified cases have an additional five "mirrored" cases which increase the number of load scenarios to 10. Due to the fact that the EEV cannot be Axisymmetrically attached on the rocket during launch, both directions orthogonal to the launch direction need to be considered independently when deciding on the applicable loading cases to be run. Considering this, the 10 load cases become 20 and, for the quasi-static launch loading analysis, a total of 20 load cases were evaluated and incorporated into the PCL code. The load case information can quickly be changed to account for different launch vehicles. For each sub-case the von Mises stress field data is output for all elements.

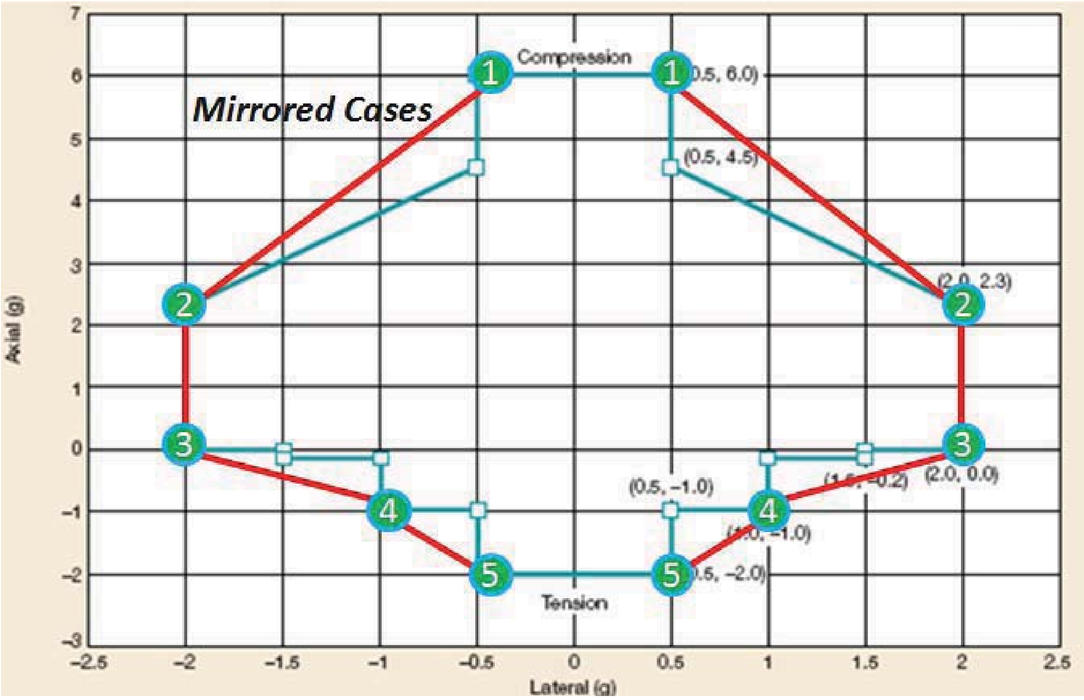

Figure 28: The inertial load envelope for one possible EEV mission launch vehicle with overlaid load case information

Structure Born Vibration Frequency Response Analysis

The frequency response analysis is intended to evaluate peak stress conditions in the EEV due to vibrations coming from the launch vehicle. A $1 m/s^2$ unit acceleration sinusoidal base excitation was applied at each attachment point. For testing and demonstration in this analysis the modal response of the vehicle is recovered from 20Hz to 400Hz. If the analyst desires a broader frequency range to be evaluated, this can quickly be changed in the PCL code. A lumped mass formulation is used. The acceleration frequency response for five different nodes was output. The node locations which are shown in Fig. 30, have been parameterized so that they remain in the same location regardless of mesh density or geometric variation. Later the settings can quickly be modified so that stress data is output for specific elements or the whole model.

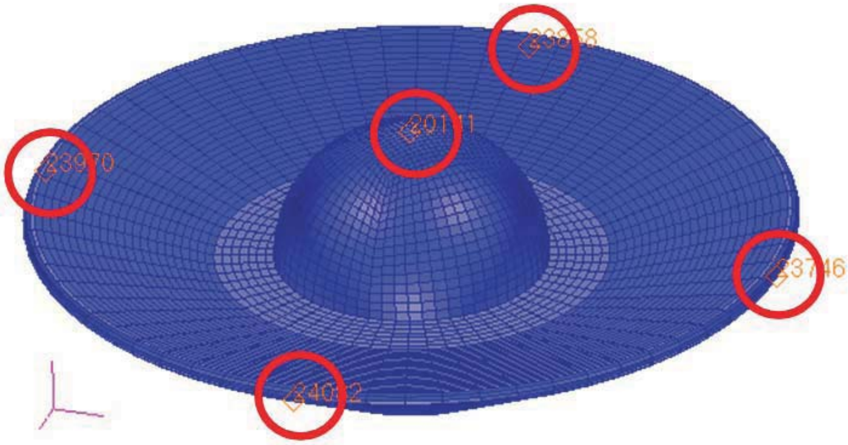

Figure 29: Node locations for acceleration frequency response output

Random Acoustic Analysis

The random acoustic analysis is intended to evaluate the structural response of the EEV due to broad spectrum high intensity noise caused by the rocket boosters during the lift off. In the more fragile light weight space structures, the high intensity noise has enough energy to create structural damage and so random acoustic analysis must be conducted. For this analysis, NASA provided a broad spectrum acoustic pressure plot for one possible launch vehicle. The plot shown in Fig. 31 is the pressure intensity in units of dB within the rocket, where the EEV will be stored during launch. To run a random acoustic analysis first, a pressure frequency response analysis must be conducted with a 1Pa pressure applied uniformly to the external surface of the EEV. Output data from the pressure frequency response analysis is then input into a separate random analysis module found in Patran. The multi-step process has been fully automated in the developed PCL code.

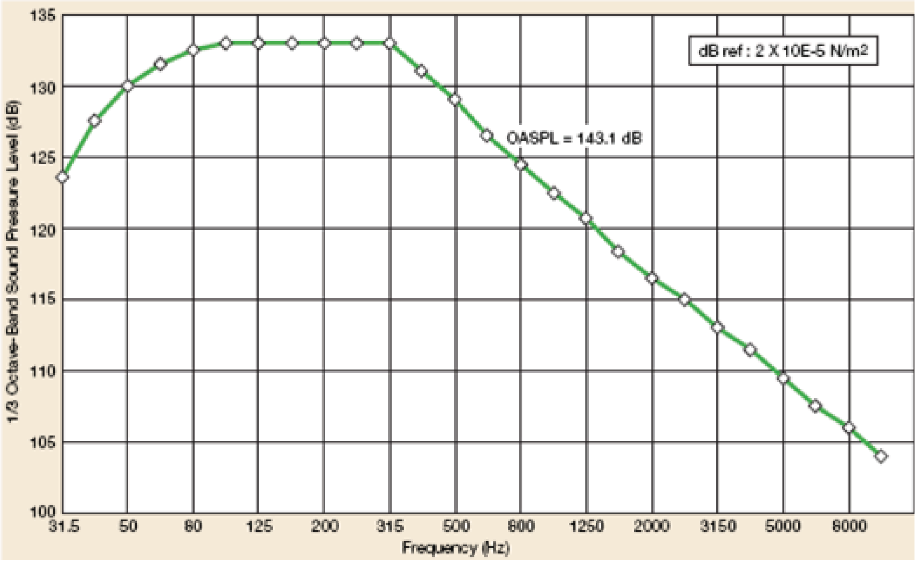

Figure 30: Sound pressure level plot from 31.5hz to 8000Hz inside one possible EEV mission launch vehicle

In order for the data in Fig. 31 to be used in Nastran it needs to be converted into pressure power spectral density (PSD) units. NASA often conducts frequency response analyses up to 2000Hz, so the spectrum from 20Hz to 2000Hz was converted into pressure PSD and is presented in Fig. 32. The data in the figure has been entered into the PCL code and can be modified if necessary to accommodate analyses for different launch vehicles. The standard BCs as defined previously are also used for this analysis. von Mises root-mean-squared (RMS) stress data for all elements is output by the solver.

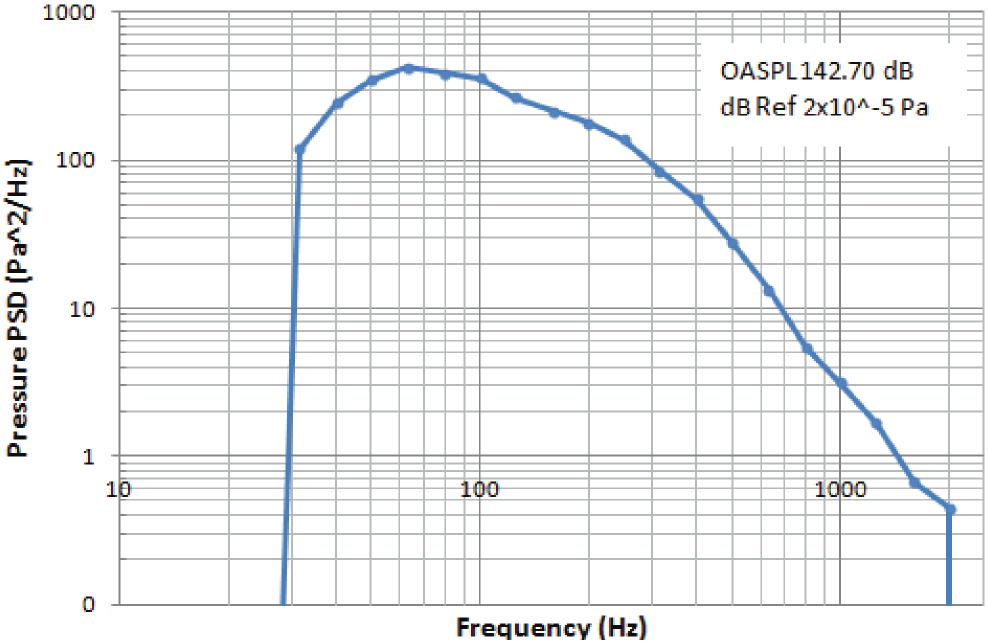

Figure 31: Sound pressure data converted into pressure PSD format from 20Hz-2000Hz

Reentry Inertial Loading Analysis

The reentry inertial loading analysis is intended to evaluate the peak structural stresses caused by the high inertial loads experienced during the early stages of reentry. Inertial loads during reentry can exceed 100g's and are possibly the most severe load case evaluated. This analysis required collaboration with aerodynamic reentry analysis team. The inertial loads for this analysis are caused by aerodynamic forces that depend on the shape of the EEV vehicle which needs to be evaluated prior to structural analysis. Other reentry conditions such as velocity and approach angle to the earth's atmosphere also affect the non-uniform pressure loading induced during reentry. To accommodate the aerodynamic requirement, a .bdf (Nastran Input file) is output from Patran through the developed PCL code and input into a separate aerodynamic solver. The solver then calculates the pressure load map on the bottom surface of the EEV and builds a Patran load case with this information. The load case information is then fed back into Patran and the developed PCL code continues the analysis with the provided load case. The EEV is in a free-fall condition during reentry and so no explicit boundary conditions are applied. In order to keep the simulation in equilibrium, first a 1m/s inertial load is applied to the EEV in the direction opposing the reentry pressure load, then the "inertial relief" setting is applied. The inertial relief setting automatically determines the correct inertial force required to exactly counteract all other forces applied in the simulation. A lumped mass formulation is used in this analysis. The von Mises stress field data for all elements are recovered from this analysis.

Model Verifications and Checks

It is recognized that that model verifications and checks are no comparison to validations against experimental data. In the future as the EEV concept becomes more mature, it is anticipated that experimental data will become available to validate the SDM. Without experimental data to check the SDM's accuracy, the SDM and developed code were continuously checked for errors and were verified throughout the development process. Good finite element modeling practices were employed and analysis techniques were verified using simple models with known solutions.

Standard NASA mandated model checks were completed on both the impact model and the SDM[13]. These checks include prescribed unit displacement checks, free-free dynamics checks, unit gravitational loading checks, and extensive element shape and formulation checks. In regard to the element shape checks, the automatic meshing portion of the developed code is optimized to produce elements with acceptable aspect ratios and curvatures for all mesh factors. With the exception of a few elements internal to the IS (which will have a negligible effect on total EEV response), all elements in the EEV were found to pass standard Nastran geometry checks. Coinciding element checks were completed and duplicate nodes were automatically removed from the model during the automated model build process. Element normals were also checked. The code is written to automatically reverse normals where necessary. As discussed in detail in the impact model design section, mass checks were completed. Mass checks were also completed on the SDM and the model mass calculations were verified independently with hand calculations.

In addition to the model verification checks, the analysis methods were tested on simpler models where results could independently and more simply verified. For the quasi-static case, a simple single element study was completed to show that correct reaction forces and stresses could be recovered from the inertial loading. For the frequency response analysis a beam model with a known exact solution was modeled and analyzed. The results from the Nastran simulation were found to closely match the hand solutions as well as results found in other FE codes. For the random acoustic analysis an aluminum cantilevered beam was independently modeled to match a tutorial found on a NASA website[14]. The results of the model that was built matched the results from the tutorial.

Structural Dynamics Model Results

To demonstrate the usefulness of the developed parametric SDM, two different parameters were manipulated and simulations were run. Mesh density and cone angle were chosen as the two parameters to be manipulated. For mesh density a single parameter was developed and named "mesh factor". The parameter is set so that only integer values can be assigned to it. For demonstration purposes, mesh factors of 1 (low density), 2 (medium density), and 3 (high density) were evaluated. Higher values can be assigned but computational time will increase exponentially. For the cone angle parameter, 20°, 30°, and 40° were evaluated. The base configuration of the EEV as presented in Fig. 24 has a mesh factor of 2 and a cone angle of 30°. Figure 33 shows how the different parameters are variations of the base configuration model located at the center of the image.

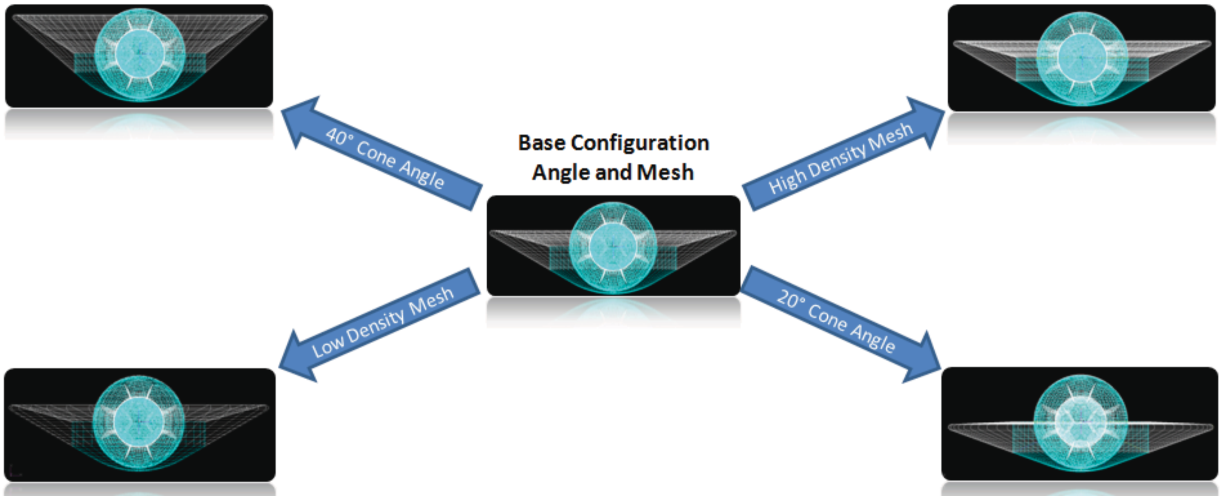

Figure 32: Diagram showing the various parameter models as variations of the base configuration model

Quasi-Static Launch Loading Results

As described previously, 20 load cases were run simply by executing the developed PCL code. Thus, by evaluating five different models together, a total of 100 different results were generated. Table A1 located in the appendix contains the complete list of results for the quasi-static analysis. The mesh factor 1 model had a max stress of 3.11 MPa, the mesh factor 2 model had a max stress of 3.38 MPa, and the mesh factor 3 model had a max stress of 3.64MPa. Trends from the mesh study showed that each successive increase in mesh density increased the maximum stress. This is a common finding in FE models when the mesh density is inadequately refined in order to fully resolve localized stress concentrations. However in the developed model this trend is caused by a different phenomena. Mesh based convergence was not achieved over this narrow range of mesh

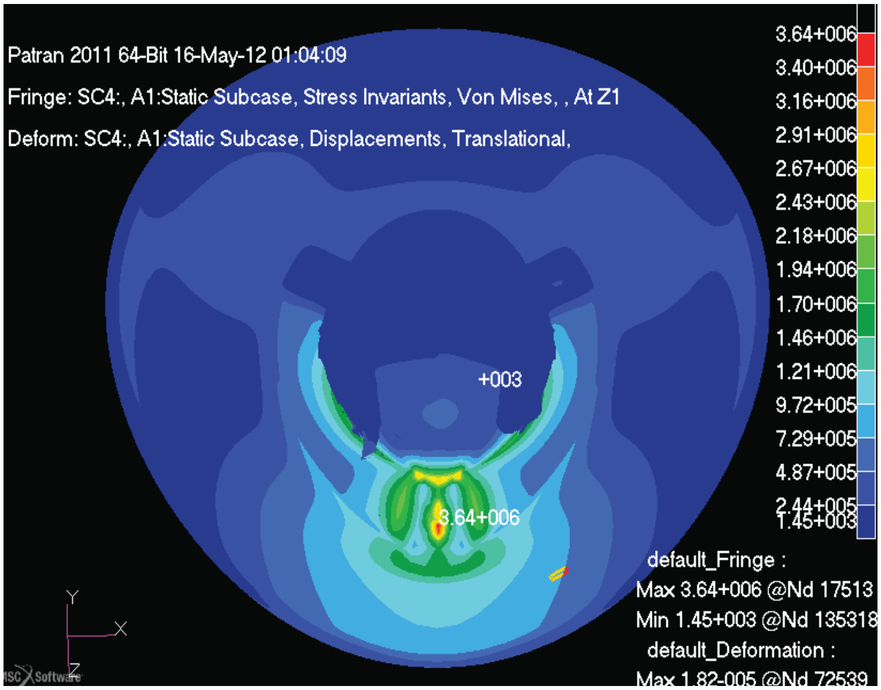

Figure 33: Stress contour plot with deformation for the high density mesh sub case with the largest max stress

samples primarily due to the complicated nature in which the boundary condition nodes are parametrically defined. Thus when the analyst is attempting to converge results based on mesh density care should be given when interpreting results near the attachment points. After the results were generated for this report, the module for assigning boundary conditions was improved to make boundary condition assignment more consistent. This should yield more predictable results in future work. Figure 34 shows the stress contour with deformation for the high density mesh case with the highest max stress.

Frequency Response Results

For each parametric variation of the model and for each orthogonal direction (X, Y, Z), a base excitation analysis was conducted via the PCL code. Also for each orthogonal direction three orthogonal acceleration response sets are generated and output from the analysis. Thus a large sample of frequency response data was generated very quickly using the developed code. Because such a huge data set was generated only a few key points from the analyses will be highlighted. The analysis shows that the largest peak response to each orthogonal base excitation was in the same direction as the excitation. The largest peak resonant response was found for the Y direction base excitation which is an excitation perpendicular to the broad circular cutout plane of the EEV.

The effect of mesh density on frequency response was investigated. In Fig. 35, the Y direction frequency response plot due to a Y direction base excitation is found. In the plot it can be seen that at a mesh factor of 1 the first resonant peak is 390Hz. At both mesh factors 2 and 3, the first resonance was reduced to 355Hz, 35Hz lower than the

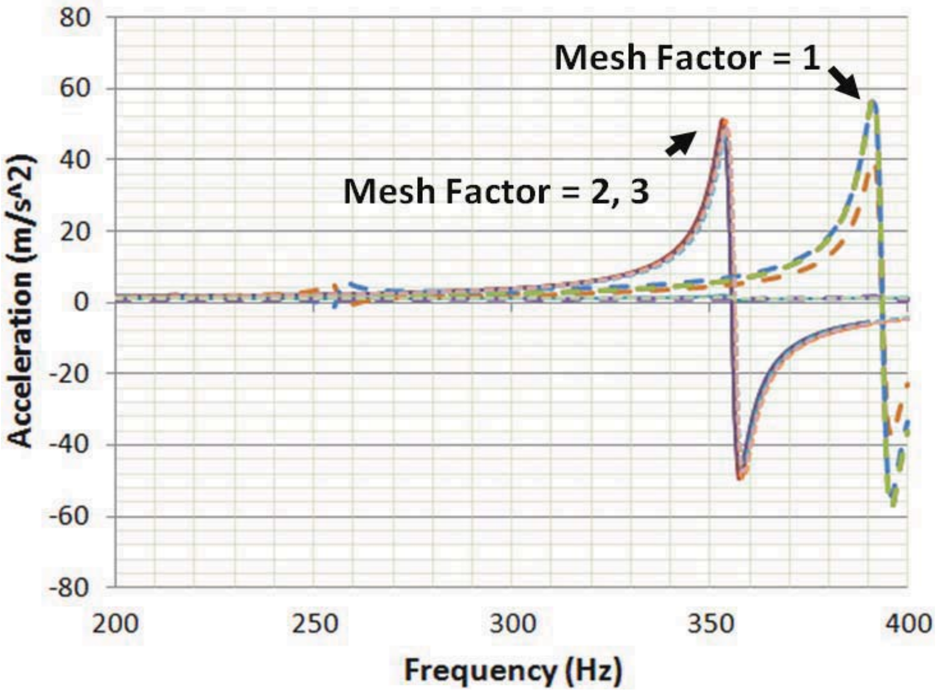

Figure 34: Y direction frequency response plot for different mesh densities

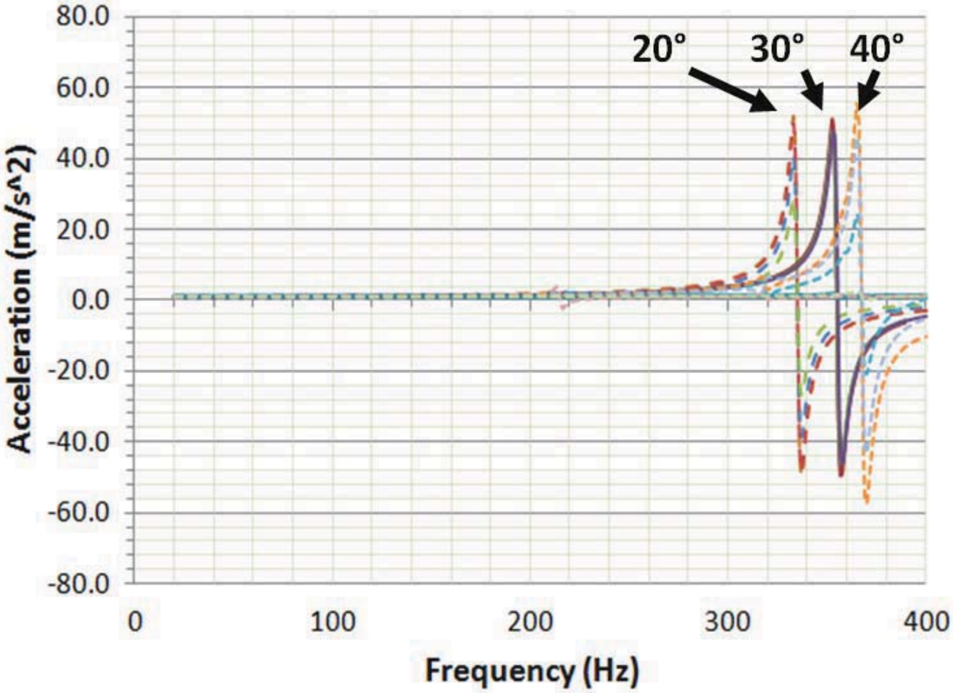

Figure 35: Y direction frequency response plot for different cone angles

results for a mesh factor of 1; a significant difference. A person familiar with finite element convergence theory might find this problematic for a lumped mass model. Although not fully described here, the reason for this unexpected reverse type convergence likely lies in the way that the boundary conditions of the test article were defined and documented, as well as the way the composite material made attachment areas were thickened to reduce localized stress concentrations. Because the frequency response curves for mesh factors 2 and 3 look almost identical, the model is considered to have reached an acceptable level of convergence for this analysis. Convergence was more easily obtained for this analysis because modal convergence is not affected by local stress concentrations.

Next, the effect of cone angle on frequency response was investigated. In Fig. 36, the frequency response plot for the three different cone angles is found. The first resonance frequency for the 20° cone angle was about 333Hz, for the 30° cone angle it was 352Hz, and for the 40° cone angle 365Hz. Thus, from the figure, it can be seen that as cone angle is increased from 20° to 40° the first natural frequency is increased but the magnitude of the resonance remains about the same for each case. Using the developed design tool, trends like this can quickly be uncovered. NASA engineers can use the developed SDM to quickly determine important cause and effect relationships in the EEV design.

Random Acoustic Results

In the same manner as the previous analyses, the random acoustic analysis was conducted on all five variations of the EEV model. The effects of mesh density on the random acoustic results were investigated. The mesh factor 1 model case had a max stress of 0.50MPa. The mesh factor 2 model had a max stress of 0.76MPa. The mesh factor 3 model had a max stress of 0.81MPa. The change between the mesh factor of 2 and 3 is only 6% compared with the change between 1 and 3 which is 38%. This is a good indicator that at this point in model development the model has a sufficient level of accuracy. If more stringent levels of accuracy are required, the mesh factor can be increased to 4 or higher. Figure 37 shows the high density mesh RMS stress contour plot. In the image, stress concentrations can be seen in red near the attachment areas. These stress hot spots are not present in the lower mesh density models as there are not enough element in the area to resolve the high stresses. It is recommended for future analyses that mesh factors of 2 or higher be used for the random acoustic analysis. Also of interest in Fig. 37 are the rings of high and low stress on the surface of the top structure of the EEV. These rings are representative of the resonance mode shape of the EEV when excited. The blue areas indicate areas of low stress (nodes) and the light blue and green areas indicate higher stress areas (peaks). When examining the results of the cone angle parameter study several trends were uncovered. For the 20° model the maximum stress was 0.80MPA, for the 30° model it was

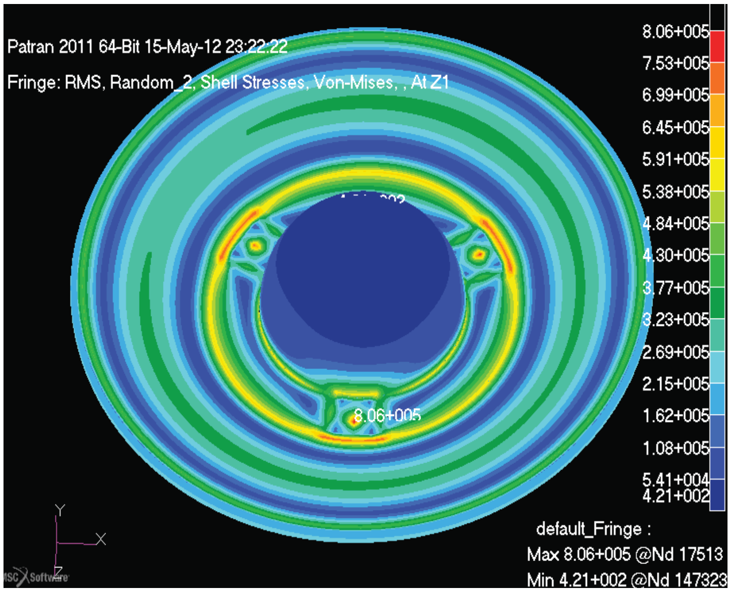

Figure 36: High density mesh RMS stress contour plot due to random acoustic pressure

0.76MPa, and for the 40° model, 0.86MPa. Beyond the peak stress values the overall stress gradients are of interest. In Fig. 38, the contour plots for the 20° case and the 40° case are presented. In the 20° model, the high stress areas are spread out fairly evenly across the surface of the EEV. However, when the cone angle parameter is increased all the way to 40°, the stress distribution becomes much more localized near the attachment points.

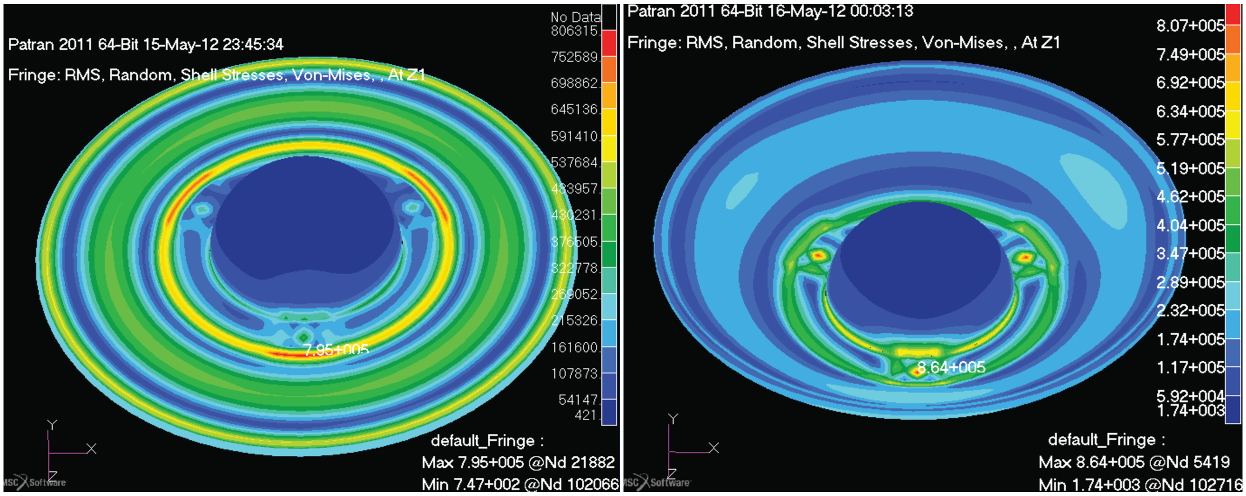

Figure 37: Low angle cone angle vs. high angle cone angle stress contour plots

Reentry Inertial Loading

The code has been prepared to accept input files from the aerodynamic code and then run them using the inertial relief technique. Test models with uniform pressure load cases have been tested but more checks need to be completed to ensure that the .bdf files are correctly output to the aerodynamic solver and that the modified files are correctly returned to code. In ongoing collaboration with NASA, more work will be undertaken to ensure this portion of the code works well and is integrated with the overall system design tool that is being developed for the MMEEV project[3].

Results Summary

The two models that were developed, when combined together form a single design tool for evaluating the fundamental structural aspects of an EEV during launch, reentry, and Earth impact. Each model was built for different FE codes to take advantage of each code's strengths.

Several sub analyses were conducted on the impact model to demonstrate the model's abilities and to support future NASA activies aiming at enhancing the EEV design. First a damping parameter intrinsic to the FE code was investigated and its effect on the crush response of the IS was determined. Second, the effects of different IS orientations on crush response were investigated. It was determined from the investigation that future simulations should use the cell wall edge orientation as the crush response in this orientation represents the weakest impact performance with the highest peak accelerations in the OS. Lastly, the model was validated against two test cases completed at the NASA LaRC facility in 2002. Very good agreement was observed between the model and the test cases. Based on the results, it is believed that the model will be effective for future use with different material properties and impact scenarios.

Four analyses were programed and automated to run in the code. A sample set of analyses was conducted on the mesh density parameter and cone angle parameter. A total of five different models were generated using the developed PCL code. For the quasi-static analysis, 100 load cases were run for 5 different potential variations of the EEV design. Stresses near the attachment points were found to be the largest in all of the models. Maximum stress based convergence was not achieved because of stress concentrations near the attachment points and the parametric method of assigning the boundary conditions. Slightly different peak stresses were found by varying the cone angle. For the structure born vibration frequency response analysis, the acceleration response due to sinusoidal unit base excitations was evaluated. Modal convergence was achieved at a mesh factor of 3. Increasing the cone angle had the effect of increasing frequency of the first resonance and natural frequency. For the random acoustic analysis, modal convergence was achieved at a mesh factor of 3. Maximum RMS stress was found near the attachment points. When increasing the cone angle, the stress contour plot changed significantly, which can be indicative of a significant change in the mode shape, subject to further investigation. Lastly, work on the reentry analysis was completed but full integration of the aerodynamic components of the analysis is still in progress. Final integration of the aerodynamic aspect of the reentry load conditions will be completed in a future phase of the MMEEV program.

High Performance Computing Integration

The ultimate goal of creating a parametric model is to run hundreds or even thousands of simulations with different parameter values so that the effect of changing each parameter can be uncovered and the best parameter values chosen. Running thousands of analyses that each take hours to complete as well as analysing their gigabytes of output is a task only suitable for high performance computing centers and clustered servers.

In some cases it has been seen that numerical models developed on one platform can output different results or even fail to run on different computing platforms. During the initial stages of HPC integration testing, some errors and discrepancies occurred. This was determined to be cause by different software versions being used for model development and then for simulation. It is recommended that when new FE code revisions become available, the results of the developed model be rechecked for consistency

The design tool was developed and tested in the CRASH Lab at Virginia Tech on a typical engineering workstation operating the Windows platform. At NASA, for the bulk of future analyses, an HPC cluster running on the Linux platform will be used. To ensure that the developed design tool will operate correctly on the NASA system, all models were checked and confirmed to run in the same manner on the NASA server as they did on the VT system. The results of each analysis for both the impact model and SDM were compared between platforms and found to be nearly identical.

Conclusion

A highly parametric design tool was developed to aid in the design of future EEVs for NASA sample return missions, the most notable of which is the Mars Sample Return mission, currently planned to launch in 2020. The developed model was designed to evaluate the impact and structural dynamic response of an EEV during launch and reentry. It is intended that the model will be integrated into a larger system level analysis tool that will allow NASA to evaluate all necessary aspects of an EEV design, including thermal and aerodynamic aspects. The developed design tool is composed of two numerical analysis modules: Module I was designed to address the highly non-linear response of the EEV during earth impact, where the second module was created to determine the structural dynamic and vibratory behavior of the vehicle during launch and reentry.

For the impact module (Module I), due to the highly dynamic and non-linear nature of the analysis, an explicit finite element code was used. Displacement, velocity, and acceleration data from the developed model were compared against two sources: two experimental tests conducted at the NASA Langley Research Center (LaRC) and an MSC.Dytran model developed in the earlier preliminary research phase. Sub-analyses including a foam material model 'damping parameter' characterization study and impact orientation study were also conducted. The parametric nature of the developed model allowed for quick modification of the model for comparison with two different impact cases with distinct geometries and material properties. The results of the developed model were shown to compare well with each of the NASA tests, thus validating the model for future simulations and different impact scenarios.

The structural dynamics module (Module II) was designed to be exceptionally parametric, giving NASA engineers the ability to investigate many EEV designs in short timeframes. In contrast to most other FE models, built using a pre-processor interface, the SDM was developed using scripts. This feature enabled rapid changes to a broad array of model parameters, which is a sophistication not found in models built through the software graphical user interface. Consequently, any vehicle characteristic can be quickly investigated, and the EEV structurally optimized for specific missions. The SDM characterizes an EEV's structural response through four separate analyses; quasi-static, frequency response, random acoustic, and reentry inertial loading analyses. To demonstrate the parametric capabilities of the model, key geometric dimensions were varied and all analyses were run. The mesh parameter study determined that local stress concentrations near the attachement points caused issues with maximum stress based convergence however, the data from the frequency response and random analyses indicated convergence was achieved at a mesh factor of 3. For the cone angle study, each analysis uncovered differerent aspects, with the most notable being that increasing the cone angle resulted in frequency shift and attenuation of the EEV's first natural mode.

The engineer has always been limited by the power of his tools. Everyday engineers make important design decisions based on incomplete test data or on the merits of limited performance metrics. These decisions often have lasting and expensive consequences for years or decades into the future. The highly parametric finite element design tool that was successfully developed attempts to change this. This tool has been tested and its efficacy demonstrated. NASA engineers now have the tools necessary to make structurally optimized EEVs and, subsequently, possess the ability to tailor their designs to cater for missions to the moon or all the way to Mars and beyond. The CRASH Lab has been privileged to be a part of these developments.

References

1. Maddock, R. W., "Multi-Mission Earth Entry Vehicle Design Trade Space and Concept Development Status," *Seventh International Planetary Probe Workshop*, Barcelona, Spain, June 2010.

2. Olynick, D., Chen, Y.K., and Tauber, M.E., "Aerothermodynamics of the Stardust Sample Return Capsule," *Journal Spacecraft and Rockets*, Vol. 36, No. 3, 1999.

3. Samareh, J. A., Maddock, R.W., Winski, R.G., Sky, B., Winski, R.G. "An Integrated Tool for System Analysis of Sample Return Vehicles," *IEEE 2012 Aerospace Conference,* pp. 1-9, Hampton, VA, 2012.

4. Kellas, S. "Design, Fabrication and Testing of a Crushable Energy Absorber for a Passive Earth Entry Vehicle," *NASA STI*, p. 1-49, Hampton, VA, 2002.

5. Bauer, N. C., Smith, B. P., Tanner, C. L., Spencer, D. A., "Multi-Mission Earth Entry Vehicle Impact Analysis," *Georgia Tech NASA Report*, pp 1-12, Atlanta, GA, 2009.

6. Billings, M.D., "Analytical Impact Entry Simulations of Energy-Absorbing Sample Return Earth Spheres Vehicle for a Mars Sample Return Earth Entry Vehicle," *NASA STI, p*. 1-86, Hampton, VA, 2002.

7. Piero, G.D., Pampolini, G., "On the rate-dependent properties of open-cell polyurethane foams," *Technische Mechanik*, 30(1-3), pp.74-84. Ferrara, Italy, 2010.

8. *Keyword User's Manual* Rev 5., Livermore, CA: LSTC Corp., 2010.

9. *MD Nastran Quick Reference Guide MD Nastran 2011 & MSC Nastran 2011 Quick Reference Guide* 2012nd ed., Santa Ana, CA: MSC Corp. 2012.

10. Performance Composites Ltd., *Mechanical Properties of Carbon Fibre Composite Materials Fibre / Epoxy Resin.*. [ONLINE] Available at: http://www.performance-composites.com/carbonfibre/mechanicalproperties_2.asp. 2012.

11. Laub, B., "Thermal Protection Concepts and Issues for Aerocapture at Titan," *AIAA/ASME/SAE/ASEE Joint Propulsion Conference and Exhibit* , pp. 1-10, Huntsville, AL, 2003.

12. Evonik Industries., *Properties of Rohacell WF*. Magnolia AR, Evonik Industries, 2012

13. FEMCI Book, *FINITE ELEMENT MODEL VALIDITY CHECKS*. [ONLINE] Available at: http://femci.gsfc.nasa.gov/validitychecks/index.html. 2006

14. FEMCI Book, NASTRAN Random Vibration. [ONLINE] Available at: http://femci.gsfc.nasa.gov/rand_vib/index.html. 2006

15. Bayandor, J., Elder, D.J. and Nguyen, M.Q., "Unification Options for the Impact and Damage Analysis Tool (IDAT)," *Technical Memorandum for Airbus Deutschland GmbH*, Cooperative Research Center for Advanced Composite Structures, 2003.

16. Mattingly, R., and May, L., "Mars Sample Returns as a Campaign," *IEEE Aerospace Conference,* Big Sky, MT 2011.

Acknowledgements

The following persons and organizations have been pivotal in the acquisition and success of this project. Sincere thanks go to all of them and also the research team at *CRASH Lab,* and *the Department of Mechanical Engineering, Virginia Tech*. Without their support this work could have not been successful. This project has been supported by the NASA LASER program under the NIA contract number NNL09AA00Z-AMA.

Project Personnel

NASA Langley Research Center (LaRC)

Dr. Sasan Armand: NASA Technical Manager

- An expert in structural dynamics and space system integration, Dr. Armand provided assistance during the SDM model development. Dr. Armand also provided critical assistance for using the NASA HPC systems.

Dr. Jamshid Samareh: Technical Director

- The technical expert on EEV design, Dr. Samareh shared his views on parameterizing the modeling process to assist in detailed development of the MMEEV in preparation for its launch in 2020. His constructive feedback and suggestions throughout the term of the project are highly appreciated.

National Institute of Aerospace (NIA)

Mr. Bo Walkley

- The NIA monitor for the project, Mr. Walkley and NIA generously involved CRASH Lab in the LASER Program, oversaw the progress, and arranged for the project Phases I and II meetings and presentations in Hampton, Virginia.

Analytical Mechanics Associates Inc (AMA)

Mr. Aaron Horning

- The technical monitor from AMA, Mr. Horning participated in weekly research meetings, and was instrumental in facilitating the AMA, CRASH Lab, LaRC and NIA collaboration and visits.

Technical Support, Code Development

Mr. Lance Proctor (NASA LaRC)

- An expert user and past developer of Nastran/Patran suite of software, Mr. Proctor, currently working at LaRC, provided critical assistance during the parametric model code and script development.

Appendix

Table 6. Max. Von Mises Stress Results from Quasi-Static Analysis

Inertial Load Cases									
Load Case					Base Design	Low Density Mesh	High Density Mesh	20° Cone Angle	40° Cone Angle
	X (g)	Y (g)	Z (g)	ID	Stress (MPa)	Stress (MPa)	Stress (MPa)	Stress (MPa)	Stress (MPa)
1	0	0.5	6	*1*	3.04	3.38	3.56	3.28	3.64
	0	-0.5	6	*1m*	3.04	3.35	3.57	3.28	3.51
	0.5	0	6	*2*	2.98	3.37	3.49	3.19	3.38
	-0.5	0	6	*2m*	3.11	3.36	3.64	3.37	3.57
2	0	2.3	2	*1*	1.23	1.36	1.38	1.27	1.63
	0	-2.3	2	*1m*	1.18	1.22	1.39	1.27	1.29
	2.3	0	2	*2*	1.85	1.32	1.27	1.03	1.4
	-2.3	0	2	*2m*	1.55	1.23	1.77	1.69	1.59
3	0	2	0	*1*	0.703	0.632	1.77	0.751	0.765
	0	-2	0	*1m*	0.703	0.632	0.838	0.751	0.765
	2	0	0	*2*	0.673	0.674	0.838	0.639	0.736
	-2	0	0	*2m*	0.673	0.674	0.663	0.639	0.736
4	0	1	-1	*1*	0.517	0.529	0.663	0.554	0.584
	0	-1	-1	*1m*	0.54	0.597	0.606	0.555	0.727
	1	0	-1	*2*	0.706	0.546	0.602	0.768	0.708
	-1	0	-1	*2m*	0.706	0.575	0.805	0.45	0.611
5	0	0.5	-2	*1*	1.02	1.1	0.556	1.09	1.14
	0	-0.5	-2	*1m*	1.02	1.14	1.19	1.09	1.26
	0.5	0	-2	*2*	1.09	1.11	1.27	1.19	1.23
	-0.5	0	-2	*2m*	0.958	1.13	1.13	1.01	1.2
Worst Case					3.11	3.38	3.64	3.37	3.64

REPORT DOCUMENTATION PAGE

Form Approved
OMB No. 0704-0188

The public reporting burden for this collection of information is estimated to average 1 hour per response, including the time for reviewing instructions, searching existing data sources, gathering and maintaining the data needed, and completing and reviewing the collection of information. Send comments regarding this burden estimate or any other aspect of this collection of information, including suggestions for reducing this burden, to Department of Defense, Washington Headquarters Services, Directorate for Information Operations and Reports (0704-0188), 1215 Jefferson Davis Highway, Suite 1204, Arlington, VA 22202-4302. Respondents should be aware that notwithstanding any other provision of law, no person shall be subject to any penalty for failing to comply with a collection of information if it does not display a currently valid OMB control number.
PLEASE DO NOT RETURN YOUR FORM TO THE ABOVE ADDRESS.

1. REPORT DATE *(DD-MM-YYYY)*
01- 06 - 2013

2. REPORT TYPE
Contractor Report

3. DATES COVERED *(From - To)*

4. TITLE AND SUBTITLE
A Comprehensive Structural Dynamic Analysis Approach for Multi Mission Earth Entry Vehicle (MMEEV) Development

5a. CONTRACT NUMBER
NNL09AA00Z

5b. GRANT NUMBER

5c. PROGRAM ELEMENT NUMBER

6. AUTHOR(S)
Perino, Scott; Bayandor, Javid; Siddens, Aaron

5d. PROJECT NUMBER

5e. TASK NUMBER

5f. WORK UNIT NUMBER
346620.04.07.01.01.02

7. PERFORMING ORGANIZATION NAME(S) AND ADDRESS(ES)
NASA Langley Research Center
Hampton, Virginia 23681

8. PERFORMING ORGANIZATION REPORT NUMBER

9. SPONSORING/MONITORING AGENCY NAME(S) AND ADDRESS(ES)
National Aeronautics and Space Administration
Washington, DC 20546-0001

10. SPONSOR/MONITOR'S ACRONYM(S)
NASA

11. SPONSOR/MONITOR'S REPORT NUMBER(S)
NASA/CR-2013-218003

12. DISTRIBUTION/AVAILABILITY STATEMENT
Unclassified - Unlimited
Subject Category 18
Availability: NASA CASI (443) 757-5802

13. SUPPLEMENTARY NOTES
This work was performed by Virginia Tech for the National Institute of Aerospace under NASA contract NNL09AA00Z with Analytical Mechanics Associates, Inc.
Langley Technical Monitor: Sasan C. Armand

14. ABSTRACT

The anticipated NASA Mars Sample Return Mission (MSR) requires a simple and reliable method in which to return collected Martian samples back to earth for scientific analysis. The Multi-Mission Earth Entry Vehicle (MMEEV) is NASA's proposed solution to this MSR requirement. Key aspects of the MMEEV are its reliable and passive operation, energy absorbing foam-composite structure, and modular impact sphere (IS) design. To aid in the development of an EEV design that can be modified for various missions requirements, two fully parametric finite element models were developed. The first model was developed in an explicit finite element code and was designed to evaluate the impact response of the vehicle and payload during the final stage of the vehicle's return to earth. The second model was developed in an explicit code and was designed to evaluate the static and dynamic structural response of the vehicle during launch and reentry. In contrast to most other FE models, built through a Graphical User Interface (GUI) pre-processor, the current model was developed using a coding technique that allows the analyst to quickly change nearly all aspects of the model including: geometric dimensions, material properties, load and boundary conditions, mesh properties, and analysis controls. Using the developed design tool, a full range of proposed designs can quickly be analyzed numerically and thus the design trade space for the EEV can be fully understood. An engineer can then quickly reach the best design for a specific mission and also adapt and optimize the general design for different missions.

15. SUBJECT TERMS
Dynamics; Entry vehicle; Impact; Mars return

16. SECURITY CLASSIFICATION OF:			17. LIMITATION OF ABSTRACT	18. NUMBER OF PAGES	19a. NAME OF RESPONSIBLE PERSON
a. REPORT	b. ABSTRACT	c. THIS PAGE			STI Help Desk (email: help@sti.nasa.gov)
					19b. TELEPHONE NUMBER *(Include area code)*
U	U	U	UU	60	(443) 757-5802

Standard Form 298 (Rev. 8-98)
Prescribed by ANSI Std. Z39.18